ChemElectroChem

Review
doi.org/10.1002/celc.202400159

Chemistry Europe
European Chemical Societies Publishing

www.chemelectrochem.org

Insights into the Single Atom and Support Interaction in Electrocatalytic Oxygen Evolution Reaction

Carsten Walter[+],[a] Ajit Kumar Singh[+],[b] Tobias Sontheimer,[c] Arindam Indra,*[b] and Prashanth W. Menezes*[a, d]

Electrochemical water oxidation with single atom catalysts (SACs) has garnered immense interest because of their high atom utilization, extraordinary activity, and elucidation of the reaction mechanism. In SACs, while the atomic sites offer active centers for substrate binding and reaction intermediates, their interaction with the solid support is crucial for the stabilization and enhancement of catalytic activity. Coordinated elements surrounding the atomic site create a ligand-like environment that influences electrochemical properties. As a result, tuning the coordination environment of SACs allows for modulation of their oxygen evolution reaction (OER) activity. In light of this, the question arises: What is the role of the support in stabilizing single atoms (SAs) and controlling their electrochemical activity during water oxidation? This review addresses this question using recent examples. Spectroscopic characterizations and density functional theory (DFT) calculations provide a direct answer: In SACs, the atomic centers exhibit strong interactions with the support via neighboring atoms, influencing OER activity.

1. Introduction

Commercial applications of electrocatalysts are severely constrained by their presence in bulk or nano-scale forms, resulting in poor atom economy and high cost.[1] Therefore, the most promising approach is to utilize each atom of the catalysts by atomic-scale design. Consequently, reducing the size of the bulk material to the nanoparticle (np) to a SA can significantly boost its activity and increase its atomic utilization (Figure 1).[3–5] Increased atom utilization and lower costs in industrial applications are made possible by the high dispersion of the active centers in SACs.[1,6–9] SACs improve the inherent activity of active sites due to their low-coordination environment and charge-transfer effect via improved metal-support interaction.[10–13] Additionally, SACs serve as an excellent model for understanding reaction mechanisms and structure-activity relationships, which can be applied to developing more efficient catalysts.[4,9,14]

The term "SAC" was first used in 2011 and rapid advancements in this area have been observed over the past decade.[15,16] In this context, studies on SACs derived from different precursors have been reported.[8,17–20]

SACs are atoms of any element whether non-metal, halogen, metal, or metalloid, that are directly bonded to a solid support through various means (e.g., adsorbed, immobilized, restricted, etc.) and are, therefore, isolated from other atoms. The degree of hybridization between the electron density of the SA and the host elements depends on the nature of the interaction and the extent of orbital overlap between the two.

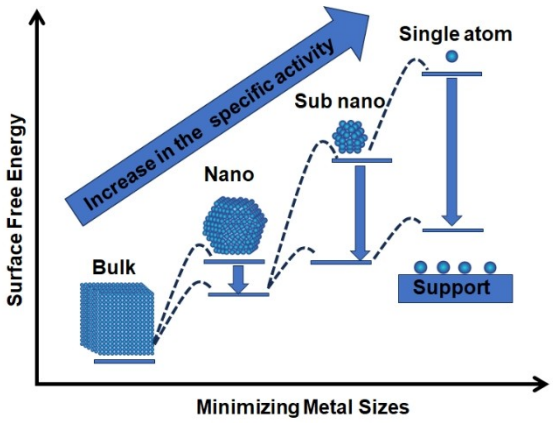

Figure 1. The illustration showing the variation in the surface free energy and specific activity with the decrease in the particle size. Modified with permission from ref. [5], copyright 2013, American Chemical Society.

[a] *Dr. C. Walter,[+] Dr. P. W. Menezes*
Material Chemistry Group for Thin Film Catalysis – CatLab
Helmholtz-Zentrum Berlin für Materialien und Energie
Albert-Einstein-Str. 15, 12489 Berlin, Germany
E-mail: prashanth.menezes@helmholtz-berlin.de

[b] *A. K. Singh,[+] Dr. A. Indra*
Department of Chemistry
IIT (BHU)
Varanasi, UP-221005, India
E-mail: arindam.chy@iitbhu.ac.in

[c] *Dr. T. Sontheimer*
Strategy Department of Energy and Information,
Helmholtz-Zentrum Berlin für Materialien und Energie,
Hahn-Meitner-Platz 1, 14109 Berlin, Germany

[d] *Dr. P. W. Menezes*
Department of Chemistry
Technical University of Berlin
Straße des 17 Juni 135. Sekr. C2, 10623 Berlin, Germany
E-mail: prashanth.menezes@mailbox.tu-berlin.de

[+] *Equally contributed to this work*

Being highly atom-efficient, with clearly defined active sites and an unsaturated coordination environment, SACs have shown outstanding selectivity and activity.[14] The typically positive charge on the individual atomic sites, along with the absence of metal-metal bonding in an unsaturated coordination environment, high surface energy, and quantum size effects can distinguish SACs from other nanocatalysts. The novel geometric and electronic features of SACs considerably alter interactions with reaction molecules and intermediates during the catalytic process, improving catalytic activity.[12,13]

SACs offer the properties of both heterogeneous and homogeneous catalysts, providing excellent stability and simple separation from reaction media like heterogeneous catalysts, as well as approximately 100% atomic utilization like homogeneous catalysts.[18,21,22] The improved catalytic activity of SACs was attributed to the tuned electronic structures originating from the strong electronic and other interactions between the atomic sites and the support.[12,23,24] Furthermore, atomic dispersion of the SA and unsaturated coordination environments are crucial for the adsorption and activation of reactants on the catalytic sites, reducing the energy barrier of electrochemical reactions.[6] The high surface energy of SAs often leads to agglomeration of the particles, necessitating anchoring on a solid support to prevent this phenomenon.[14,25,26] Various solid supports, such as layered double hydroxides (LDHs),[26] metal oxides,[27] phosphides,[28,29] chalcogenides,[30,31] carbon-based materials,[10] metal-organic frameworks, covalent-organic frameworks, etc., have been used to successfully anchor SAs. These anchored SAs have then been used to catalyze a wide variety of thermochemical, electrochemical, and photochemical reactions.[12,13,23,32]

The structure of active sites, composed of SAs, is directly influenced by the choice of support material. The bonding environment of deposited SAs differs significantly from that of

Carsten Walter is currently working as a postdoctoral researcher in the group of Dr. P. W. Menzes at CatLab of the Helmholtz–Zentrum Berlin für Materialien und Energie. He obtained his Ph.D. in 2019 from the Technische Universität Berlin, Germany under the supervision of Prof. M. Driess and Dr. P. W. Menezes on bioinspired heterogeneous catalysts for water oxidation. His research interests include the synthesis of functional materials for energy applications and their structure-activity relationship.

Prashanth W. Menezes is head of the materials chemistry for thin-film catalysis group at CatLab of the Helmholtz–Zentrum Berlin für Materialien und Energie and head of the inorganic materials group at Technische Universität Berlin. He received his Ph.D. from Max Planck Institute for Chemical Physics of Solids in Dresden, from where he moved to Technische Universität München and then to Technische Universität Berlin to work on energy catalysis. His research focuses on the design, development, and structural understanding of novel unconventional catalysts in heterogeneous catalysis, especially in the area of redox oxygen catalysis, (photo)electrocatalytic water-splitting as well as electrochemical redox reactions.

Tobias Sontheimer heads the Strategy Department for Energy and Information at the Helmholtz-Zentrum Berlin (HZB) and has been helping to shape the transformation of the energy sector for more than fifteen years. In his current role, he is responsible for research and development for green hydrogen technologies and sustainable aviation fuels. From 2014 to 2020, he was Chief Research Manager for the Helmholtz Association's national energy R&D portfolio. Tobias Sontheimer studied physics at RWTH Aachen University and Harvard University and completed his doctorate in the field of renewable energy technologies as a scholarship holder of SCHOTT AG.

Ajit Kumar Singh is a Ph.D student in the Department of Chemistry, IIT (BHU), India. He received his B.Sc and M.Sc degree from Banaras Hindu University. As a Ph.D student, he joined the group of Dr. A. Indra at IIT (BHU). His research focuses on electrochemical and photocatalytic energy conversion using transition metal-derived catalysts and understanding the reaction mechanism using various spectroscopic methods.

Arindam Indra is an Assistant Professor in the Department of Chemistry, IIT (BHU), Varanasi (India). He pursued his Ph.D. from IIT Bombay (Mumbai, India) on solid-supported nanocatalysts for selective organic transformation reactions. After Ph.D, he joined Technische Universität Berlin (Germany) as a postdoctoral fellow and worked in the field of bioinspired energy conversion. Then he moved to Hanyang University (Seoul, Republic of Korea) as an Assistant Research Professor and developed self-supported catalyst systems for electrochemical water splitting. Currently, his group works in the area of metal-organic framework-derived catalysts focusing on electrochemical and photocatalytic energy conversion processes.

constituent atoms in np's, as all the other atoms attached to them are not of the same element. These differences in charge distributions affect the activity of the SAC. Furthermore, tuning the electronic structures of individual atoms is achievable through metal-support solid interaction or confinement by neighboring bonding atoms.[10–13] Additionally, heterogeneous catalysts comprised of isolated SAs can exhibit diverse catalytic activity across a wide range of chemical reactions, offering a novel approach to optimizing atomic utilization.

Our attention is directed towards the unique structural features and electrochemical properties of SACs, particularly their exceptional performance as catalysts in OER and the associated investigations into their mechanisms. Recognizing the vital role of synthesis in understanding how structure influences properties, we also provide a concise overview of different methods used to tune the dispersion of SAs on various surfaces. Additionally, we discuss cutting-edge microscopic and spectroscopic methods capable of visualizing this atomic arrangement.

In this context, recent reviews have covered the synthetic protocols of SACs, surface coordination of SA, fine-tuning of the microenvironment, elemental diversity, and applications in electrochemical processes. These reports summarize the current state of SACs and comment on their potential future growth, providing an in-depth overview of the field as a whole. However, none of these reviews have discussed the behavior of SACs during the OER. Compared to conventional catalysts based on np's, SACs possess distinct advantages due to their size, structural effects, and strong interactions with the support material, which significantly affect OER activity. This review highlights the latest advancements in synthesizing and characterizing SACs, examines their performance in OER, and explores the interaction of SACs with support under OER conditions (see Figure 2).

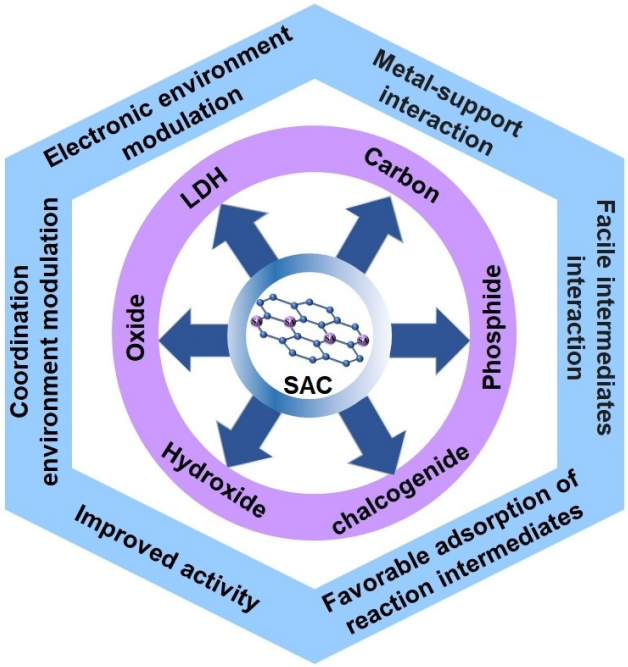

Figure 2. The objectives of the present review.

2. Challenges in OER and the Role of Catalysts

For hydrogen production via water splitting, a suitable design of electrocatalysts for OER is essential.[33] The large overpotential and high activation barrier of the OER significantly restricts the large-scale synthesis of H_2 through water splitting.[34] Moreover, the slower kinetics of the OER limit its applicability in metal-air batteries and fuel cells.[35,36] However, the reaction barrier for OER can be lowered by employing an effective electrocatalyst.[36] Due to their strong catalytic efficacy, commercially available catalysts based on oxides of noble metals like Ru and Ir are frequently utilized for the OER.[37,38] The catalysts based on noble metals have limited large-scale uses due to their instability, high cost, and poor abundance.[36,37] Therefore, developing a highly efficient, stable, cost-effective catalyst is imperative.

The stability and efficiency of the OER electrocatalyst depend on its structure and electronic properties.[39,40–42] In OER, the mass transfer process involves solid, liquid, gas phases and the effectiveness rely on how reactants and intermediates are bound on the catalyst's surface. Electrocatalysts were designed with abundant catalytic active sites,robust mechanical strength, and good electrical conductivity. Extensive research aims to find the highly active OER catalysts and elucidate the fundamental activity descriptors governing the OER performance. Several activity descriptors have been proposed to design effective transition metal oxide OER catalysts rationally.[36,43–45] These include the binding of the reaction intermediates on the surface of the catalyst, the number of the 3d electrons, and the e_g* occupancy.[45,46] The antibonding e_g* orbitals filling can be correlated to the adsorption enthalpy of O-containing intermediates and hence the OER activity of the catalysts. The broadening of the e_g* orbitals also facilitates the delocalization of the electron density and its overlap with the reaction intermediates. The number of electrons in the e_g* orbitals also controls the structural features of the catalyst.[46] For example, unevenly occupied e_g* (e_g^1 and e_g^3) leads to Jahn-Teller distortion, which in turn introduces disorder in the catalyst structure.

The d-band center theory was also applied as an indicator for the free energy change. The energy contributed by the d-band electrons is mainly composed of bonding and antibonding states, leading to the Pauli repulsion between adsorbates and 3d, 4d, and 5d TMs.[46] A positive shift of the d-band center toward the Fermi level suggests a stronger interaction, whereas a negative shift of the d-band center indicates a weaker one with the intermediates. Near edge X-ray absorption fine structure (NEXAFS) and DFT calculations showed that the electrocatalytic activity varied with the d electron configuration.[47] The DFT calculation for Fe, Co, and Ni SA on N-doped graphene showed that the reaction intermediates prefer Fe or Co site to C during OER to follow a single site mechanism. In contrast, Ni-SA follows a dual-site mechanism where O* and

OH* prefer the C site and OOH* is adsorbed on the Ni site. Additionally, Ni-SA had the lowest O_2* desorption energy barrier.

The DFT calculations for SA, such as Cr, Mn, Fe, Co, Ni, Cu, and Zn on C_3N_4 support showed the strongest binding of Fe, Ni, and Co with support to attain better stability.[48] The stability of SACs was qualitatively confirmed from the electron density differences at a certain cut-off value. The rate-determining step (RDS) for Ni_1–C_3N_4 is the O* formation step, which is different from the Co_1–C_3N_4 and Fe_1–C_3N_4 models, where the OOH* formation step is the RDS. This difference was explained by the difference in d-band position. Qualitatively, a higher d-band position (e.g., Fe_1–C_3N_4 model) leads to a stronger OH* adsorption.

A theoretical study examined the surface charge transformation of Au_1/NiFeOOH-NiFe LDH with O*.[49a] Theoretical calculations showed that Au's d orbitals had 2 electrons and O's p orbitals had 4/3 electrons. Au's five degenerated d orbitals are reallocated after adsorption on O. Hybridization of Au's dz^2 and O's p_z orbitals results in energetically distinct σ bonding and σ* antibonding states at −5.6 eV and 0.2 eV, respectively. The charge density surrounding Au's ring region parallels the surface due to d orbital redistribution. The integrated charge density difference causes a net Au-to-LDH charge redistribution of 0.32 eV, which transfers to surrounding O, Ni, and Fe atoms, facilitating OH^- adsorption and changing the adsorption energies of O* and OOH* intermediates, resulting in a low overpotential in the rate-limiting step from O* to OOH.[49a]

The spectroscopic and density functional theory calculations of the Au SA on high-entropy MnFeCoNiCu-LDH demonstrated that the introduction of Au atoms and the formation of the O vacancies lead to an upward displacement of the O 2p band toward the Fermi level. This interaction also destabilizes the metal-O bond and initiates the LOM that can break the theoretical limit of the conventional AEM and enhance the oxygen evolution reaction. Due to this, Au on high entropy MnFeCoNiCu-LDH required an overpotential of 213 mV to achieve a current density of 10 mA cm^{-2}. Furthermore, it displays the significant performance of 732.925 A g^{-1} at an overpotential of 250 mV in a 1.0 M KOH solution. In addition, it exhibits excellent stability when operated continuously for 700 hours at an approximate current density of 100 mA cm^{-2}.[49b] This study also shows that the activity of the Au-based SAC is one order of magnitude higher than that of the corresponding nanoparticles or sub-nanometer cluster materials. The SAC offers better interaction with the support compared to the nanocatalyst, which results in different catalytic activity compared to nanocatalysts. Further, the SAC outperforms nanocatalysts in terms of surface exposed sites and atomic efficiency. As a result, SACs allow maximum utilization of atoms for reactant that boosts the catalyst's activity compared to the nanocatalyst. The previous study showed that reducing the size of gold nanoclusters from 140 to 11 atoms affects electrocatalytic ORR activity. Thus, reducing a catalyst to an atomic level may improve electrocatalytic performance. Furthermore, the isolated active sites are evenly dispersed, giving a great platform for investigating structure-performance correlations in molecular and atomic details.[49b] Zhu et al. found an improvement in the HER activity by SA Pt at VS_2 compared to the Pt cluster at VS_2 and Pt nanoparticle at VS_2. They observed improvement in the mass activity of SA at 200 mV; SA Pt showed better mass activity at 22.88 A mg Pt^{-1}, which is 12 times higher than the mass activity of the commercially available Pt/C (1.87 A mg Pt^{-1}).[50] Thus, understanding the correlation between activity and the distinctive properties of active sites is paramount. Such insights enable scientists to develop state-of-the-art electrocatalysts that enhance OER activity.

Exploring methods such as tuning metal elements, regulating crystalline or electronic structures, defect engineering, and introducing conducting substrates have been investigated to enhance the activity of transition metal-based materials, particularly Fe, Ni, and Co compounds, which serve as benchmark electrocatalysts.[36,51] However, surface reconstruction and active site leaching during the electrocatalytic process drastically reduce stability.[41,42,52] Furthermore, under electrochemical conditions, these materials are agglomerated during OER, leading to poor atomic utilization efficiency that affects the overall activity of the catalyst. Although these OER catalysts have very modest overpotentials, the active sites are typically np-sized and sparsely scattered at the most prominently exposed facet or edge sites. This leads to a partial loss of electrocatalytic activity and the waste of catalysts since the interior active sites cannot be used completely.

Further, OER is a pH-dependent process and proceeds via different mechanism pathways at different pH.[53] Compared to an acidic media, alkaline OER is easier. Based on kinetic investigations and thermochemical DFT studies, several probable reaction mechanisms have been proposed, and the adsorbate evolution mechanism (AEM) and the lattice oxygen oxidation mechanism (LOM) are the most frequently recognized mechanisms for OER.[36,53,54] As it is generally understood, OER occurs via an adsorbate evolution mechanism (AEM).[53,54] It is usually accepted that OER in alkaline solutions occurs via AEM, which involves four concerted proton-electron transfers (CPET).[36] The OER in an alkaline medium initiates the diffusion of OH^- from the electrolytic solution and its subsequent adsorption on the electrocatalyst surface to form *OH, *O, and *OOH intermediates. Further, the deprotonation and desorption of *OOH takes place to form O_2. Plenty of original papers and reviews have already described the mechanism of OER in detail.[36,53,54]

3. Catalyst Structure: Transition Metal vs Noble Metal

Excellent OER activity is observed for oxides of noble metals such as Ir and Ru throughout all potential ranges. Because noble metal catalysts are rare and expensive, their practical applications are limited.[43] The approaches that have been used as potential workarounds for this restriction are synthesized electrocatalysts based on transition metals or reducing the

number of noble metals used while maintaining performance.[55] The earth-abundant 3d transition metals derived oxides, (oxy)hydroxides, sulfides, selenides, phosphide, perovskites, etc., and molecular catalysts were explored for electrocatalytic OER.[56] The transition metal electrocatalysis operates well in alkaline conditions.[43] However, these catalysts are not stable in the long run.

While progress has been made, attaining a high mass activity for OER catalysts with high stability faces various challenges. The development of SACs represents a pivotal breakthrough in materials chemistry, promising new horizons for effective OER catalysts. Over recent years, various studies have also highlighted the great potential of SACs based on noble metals and transition metals for the OER.[4,5,19,20,57–59] Among these, a diverse array of host structures continues to expand including metal-organic frameworks (MOFs),[60] covalent-organic frameworks (COFs),[61] sulfides,[62] phosphides,[2,63] selenide,[30] hydroxides,[64,65] LDHs,[26,45,66] and carbon-based materials.[12,57] Further, SAC serves as a useful model for shedding light on reaction processes and structure-activity relationships, which can be used to design more efficient catalysts for OER.[61] Since the SAC has a different geometric configuration and electronic structure from conventional catalysts, particularly when compared to metal atoms valence shell electronic structure, it possesses unexpected and exciting physical and chemical capabilities due to which it shows improved electrocatalytic activity compared to the traditional electrocatalyst.[17,33]

4. Synthesis of SACs

As previously discussed, SACs are crucial for achieving highly efficient OER. Despite certain SACs meeting commercialization requirements due to their high activity, their limited stability poses a major challenge in practical applications.

In SACs, the metal-metal interaction often outweighs the metal-support interaction, potentially leading to catalyst deactivation during synthesis and catalytic processes.[23] Hence, the synergy between the metal and the support is greatly important for enhancing electrocatalysis by SACs. This interaction smoothens the transfer of the electron from metal atoms to the solid support, thereby regulating the electronic structure of the SA.[12,24] The electrocatalytic capabilities of a SAC are profoundly influenced by its local coordination environment, including the number and shape of coordination components. Various stabilization methods have been developed to reinforce this interaction, enabling the effective and convenient fabrication of SACs. Within metal-based SACs, individual metal atoms form strong attachments to supports such as carbon materials, metals, LDH, sulfide, phosphide, selenide, or metal oxides.[62] This robust bonding occurs due to particular gaps or flaws (vacancies or defects) existing on the support surface.[23] The choice of support is crucial as it actively facilitates and shapes the bond between the SA and the support.

Moreover, controlling the loading quantity of metal sites on SACs is crucial to prevent aggregation, which could compromise overall catalytic efficiency despite individual atoms demonstrating the high activity necessary to maintain the SA configuration. Therefore, the development of highly dispersed SACs also requires strong interaction between the atomic site and support. Carefully planned synthetic techniques that disperse and isolate precursors on an atomic scale are imperative to form SAs and prevent their agglomeration.[23]

The fundamental aspect of stabilizing the catalytically active species of SACs lies in establishing robust interactions between the SAs and their support.[12] This strong interaction prevents isolated metal atoms from clustering together, ensuring stability and optimal dispersion. This interaction mainly stems from the redistribution of electrons between the SA and the support, significantly influencing the electronic structure and catalytic performance.[12]

Optimizing precursor and support materials and controlling the synthesis procedures are pivotal in fine-tuning these interactions and fabricating high-performance SACs. Several methods have been utilized to produce SACs, encompassing approaches such as the wet chemical method, galvanic-replacement method, atomic layer deposition (ALD), and high-temperature pyrolysis.[10,21,67] Among these techniques, atomic layer deposition (ALD) typically involves costly equipment and yields lower outputs, which are less conducive to large-scale manufacturing.[5,23] Presently, wet-chemical routes, like coprecipitation and impregnation methods, are considered highly promising and extensively adopted due to their simplicity in operation and potential for large-scale synthesis.[57,59]

4.1. Wet Chemical Method

The most straightforward approach to synthesizing SACs is wet chemistry, which is promising for widespread application because of its simplicity.[57,59] In this method, metal atoms are chemically coordinated to certain supports by ion exchange or chemical impregnation method, defect engineering, spatial confinement chemical bonding, coordination design, calcination, and thermal or photo energy reduction. To confirm the uniform dispersion of isolated metal atoms, it is crucial to increase their interaction with the support. Due to the high surface energy, SAs tend to aggregate into clusters if the coordination between the metal atoms and the support is not optimized, which might hinder preparation and/or catalysis.

For example, Ir SA has been loaded on β-$Ni(OH)_2$ by vacancy-assisted approach.[68] HAADF-STEM showed that Ir was uniformly deposited on the vacancy-rich $Ni(OH)_2$ and 5.81 wt% Ir-SA loading on β-$Ni(OH)_2$ was achieved. Using the same synthesis technique, different SACs (M1 = Ir, Pd, Rh, Ru, Mo, or W) with varying ratios from 2.60–9.11 wt% could be synthesized on $Ni(OH)_2$ by vacancy-assisted approach.[68] Similarly, Sun et al. took advantage of the special anchoring sites in layered double hydroxides (LDHs) and prepared monoatomic Ru sites on anchored cobalt iron LDHs (CoFe-LDHs) nanosheets for efficient alkaline OER.[26] The choice of metal oxide support can have a substantial influence on the formation process of SAs on the surface of the support. In particular, metal oxides that are

readily surface-reduced to form cations of lower valence have demonstrated strong metal support interaction (SMSI), which is linked to the formation of atomically dispersed species and inhibiting their aggregation.[69]

Zhang et al. used the electrochemical method for the loading of SA Ir on $Co_{0.8}Fe_{0.2}Se_2$@Ni foam and used it for alkaline OER.[31] Also, they applied this deposition method for loading different transition metal SA on different supports like metallic, oxides, phosphides, sulfides, selenides, carbon, and so on. Monoatomic Ru SAs were introduced onto a hybrid amorphous/crystalline surface of FeCoNi-LDH using a self-templating cation exchange approach.[70] The combined influence of the SA Ru atoms and the distinctive amorphous/crystalline LDH structure resulted in a remarkable OER performance.

The optimal synthesis parameters, including the support material, nature of the precursor, precursor concentration, temperature, surfactants, the degree of precursor solubility in solvents, and decomposition features, must be carefully adjusted to achieve SACs. The wet chemical approach allows relatively easy control over these parameters, and therefore simple accessibility to SACs and their distribution over the support.[71] It is the most applied approach to access SACs, and is well established, even for large-scale synthesis.[72]

4.2. Pyrolysis

As discussed above, SACs suffer from energy-induced agglomeration during the synthesis and application.[25] For instance, the stability of a SA is questionable. The physical and chemical instability has been overcome by using a SA bound with nitrogen, oxygen, sulfur, or carbon of the support[1,18,25] However, additional developments are needed in the near future to achieve performance at an industrial scale.

Nitrogen-doped carbonaceous scaffolds, including M–N_x–C moieties derived from transition metals, are being developed as an unconventional substitution of noble metal catalysts in thermo-/and electrocatalysis. The isolated atom density of M–N_x–C SACs synthesized at high temperatures from C/N containing precursors and metal salts is typically between 1.0 and 1.5 %.[73] Colligative increase of catalytic performance relies on the construction of densely populated M–N_x–C SACs, and "cooperative catalysis" is enabled by the near proximity of metal centers.

The high-temperature synthesis of SACs by using carbon support leads to low weight (%) loading of SAs. As a result, electrocatalytic activities specific to either mass or volume are less. High-temperature synthesis resulted in nanoclusters or np's when the metal content was high, limiting the loading of SAs. To overcome this, carbonizing N-containing MOFs is the most studied approach to fabricating high-density M–N_x–C SACs.[19,73,74] With its porous structure, well-defined channel structure, large surface area, structural variety, and ease of molecular functionalization, MOF is an ideal precursor for synthesizing M–N_x–C SACs.[10,19,73]

The inclusion of SAs with uniform dispersions via strong coordination, adsorption, or ion exchange is made possible by the large quantity of anchoring sites. In addition, the development of metal-nitrogen solid bonds by the different amine sites during high-temperature pyrolysis stabilizes metal atoms, resulting in atomically distributed metal sites in the SAC that are produced. As obtained, SA components from the MOF have a metal loading of approximately 1–5 weight %, improving the electrocatalytic activities specific to either mass or volume.[73] Iridium nanoclusters embedded in nitrogen and sulfur co-doped graphene (Ir-NSG) were synthesized by Wang et al. using the simultaneous two-stage heating of $IrCl_3.xH_2O$, melamine, and L-cysteine at high temperatures.[75] For all pH values, the SA Ir-SCN electrocatalyst exhibited good electrocatalytic activity towards OER. Zhao et al. synthesized football-shaped carbon spheres doped with S/N and adorned with single Ni atoms using a chemical vapor deposition technique.[76] This procedure is simple, inexpensive, and requires no need for any expensive instruments. Nevertheless, pyrolysis causes the agglomeration of individual atoms.[21,58] Therefore, in order to obtain an atomically distributed catalyst, either the precursor or the pyrolyzed product must undergo pre- or post-treatment. N-rich precursors like dicyandiamide, melamine, or dopamine should be added before heat treatment or calcination in an NH_3 environment to improve the metal loading and anchoring force. Altering the rate of precursor breakdown is another way to stop atoms from clumping together.

5. Characterizations of SACs

The development and preparation of SACs have highlighted a pressing need to decipher the intricate relationship between their coordination environments and catalytic efficacy. The performance of SACs can be greatly enhanced by delving into the nature of SA active sites, which can be revealed by the geometry and electronic structure, as well as the nature of metal atoms, adjacent coordination, and coordination number.[9] Rational designs are used to stabilize the metal atoms and prevent their agglomeration during synthesis and catalysis to improve isolated atoms' coordination environments further. Presently, the microscopic and spectroscopy analysis of SAC structures stands as the primary means to unravel the chemical and geometric coordination environments within catalysts. Such insight is a cornerstone for designing and fabricating atomic-scale catalysts, ultimately optimizing support choices and coordination environment construction strategies.

Modern characterization techniques such as scanning tunneling microscopy (STM) and aberration-corrected high-angle annular dark field scanning transmission electron microscopy (HAADF-STEM) have been employed to understand the distribution of the SACs on the support.[33,77–79] X-ray absorption near-edge spectroscopy (XANES), extended X-ray absorption fine structure (EXAFS) spectroscopy, Fourier transform infrared spectroscopy (FT-IR) using CO as probe and near-edge X-ray absorption fine structure (NEXAFS) can reveal further details on the oxidation states and coordination environment of the individual atoms.[60,77,80–83] Combining morphological data with structural characterization can verify the presence of SAs. These

characterization strategies are also highly important to learn about the nature of catalysis using SACs.

5.1. Electron Microscopy

Detecting SAs in high-resolution transmission electron microscopy (HR-TEM) is difficult due to their sensitivity limitations.[84,85] Rather, this restriction provides circumstantial evidence of a structure consisting of a SA. One advantage of STEMs over TEMs is the ability to concentrate electron beams to spots in the 0.05–0.2 nm range, which is significantly smaller.[33] STEM reveals the SA's atomic distribution state, structure, and morphology.[85] The Z-value of the elements in the sample produces phase contrast for the identification of SACs.[85,86] When there is a substantial atomic number difference between the surrounding elements and the atomically dispersed metals, it is easier to detect them since a high Z-contrast enhances the resolution of the image.[87]

A HAADF-STEM detector is frequently employed for lower Z-contrast.[81,86] The wavelength of an electron beam accelerated to 100 keV is 0.037; however, the aberration of the magnetic lenses limits the resolution of STEM to the sub-nanometer scale.[33] The improvement of the resolution of STEM to the sub-angstrom level, aberration-corrected STEM (AC-STEM) was introduced.[33,79] Therefore, the AC-STEM has been frequently used to investigate SACs due to its sub-angstrom resolution. It should be mentioned that the electron beam's energy can induce SA to hop and move dynamically, which could result in inaccurate pictures of atomic features. As a result, it is important to take precautions when conducting AC-STEM analysis and use test samples with a high tolerance for the electron beam. Z-contrast imaging facilitates instantaneous image interpretation by differentiating dense features from less dense ones. HAADF-STEM images show elements brightening as their atomic numbers increase.[81] AC HAADF-STEM reveals the atomic structure of SACs, metal-support interactions, and active areas below the surface.[81,88] It can directly see the location and distribution of single and dual atom sites, thus providing empirical proof of their existence.[88] When combined with DFT, STEM simulation can provide exquisite detail about the architecture of SACs.[33] Lattice vacancies can also be detected by analyzing the image intensity differences produced by the HAADF-STEM.[33] Atomic-scale mapping of individual atoms using AC-HAADF-STEM analysis can be used to determine their local stoichiometry.

The electronic structure and elemental composition of SACs can be better understood by conducting linear and planar scans with energy dispersive spectroscopy (EDS) and electron energy loss spectroscopy (EELS).[33,77,88] EELS provides information about the catalysts' electronic structure, stoichiometry, and energy levels.[81,89] Since EELS relies on electrons striking on the catalyst surface, the experiment must be performed on TEM or STEM.[33] An increased voltage electrical source and selectively placed orbital electrons can achieve a 0.1 nm precision in the EELS under ideal conditions.

Wang et al. explored Ir SA on nickel phosphide for alkaline OER. HAADF-STEM along the [001] zone axis showed that the Ir atoms are evenly distributed throughout the $Ni_{12}P_5$ crystal structure (Figure 3a).[2] Z-contrast images displayed a homogeneous distribution of Ir atoms throughout the $Ni_{12}P_5$ lattice (Figure 3b). Both simulated and experimental images demonstrated that Ir atoms occupy the Ni position of the $Ni_{12}P_5$ (Figure 3b–c). EDS mapping showed that Ir atoms are uniformly dispersed (Figure 3d). Similarly, HAADF-STEM images of IrSA-Ni_2P particles show brighter, separated iridium atoms along the [101] zone axis (Figure 3e).[2] The experimental and simulated models confirmed that Ir is present at Ni sites of the nickel phosphide. In agreement with HAADF images, atomic EDS mapping of IrSA-Ni_2P showed a high distribution of the Ir in the nickel phosphide (Figure 3f–h).

STEM using spherical aberration correction clearly demonstrated that SA Ru atoms were distributed randomly on the surface of CoFe-LDHs.[26] The element Ru was found to be equally distributed with the elements Co and Fe, with no evidence of local aggregation of Ru, as shown by HAADF-STEM imaging and matching elemental mapping. Similarly, the SA W-doped $Ni(OH)_2$ was mapped using EDS, which revealed that W was evenly distributed throughout the compound.[26] Single W atoms were found all over the $Ni(OH)_2$ surface, as seen in HAADF-STEM images of W-doped $Ni(OH)_2$. The aforementioned methods are among the more sensitive ones, providing additional insight into the chemical coordination environment, electronic configuration of the absorber, mode of binding, and oxidation states. The HAADF-STEM method has the drawback of only displaying nanoscale local information, which may not indicate the whole sample.

5.2. X-ray Photoelectron Spectroscopy (XPS)

The X-ray photoelectron spectroscopy (XPS) method relies on the principle of irradiating the sample with high-energy X-rays that expel the electrons from their energy levels. The emitted electrons are known as photoelectrons, providing information on the catalyst's atomic composition and electronic states.[81] In the context of SACs, the oxidation state and the electronic environment of SA sites can be unveiled by XPS.[90] Also, XPS provides insight into metal-support interactions including electron sharing and binding of SA to the support matrix. From this, we can also determine the type and strength of metal-support interactions. However, XPS cannot reliably identify the atomic dispersion of SACs; thus, it is commonly utilized in tandem with other techniques boasting atomic-scale resolution. Notably, the loading of SAs onto support induces a shift in the support's peak, owing to the modulation of the support's electronic environment.[80,90] For example, loading of the SA Ir on CoFe-LDH/rGO leads to shifting Fe^{III} and Co^{II}/Co^{III} peaks compared to the CoFe-LDH/rGO. The shift in the XPS peak of the Co and Fe indicates a significant interaction between Ir and Co/Fe in CoFe-LDH/rGO support by forming Ir–O–M bonds.[91]

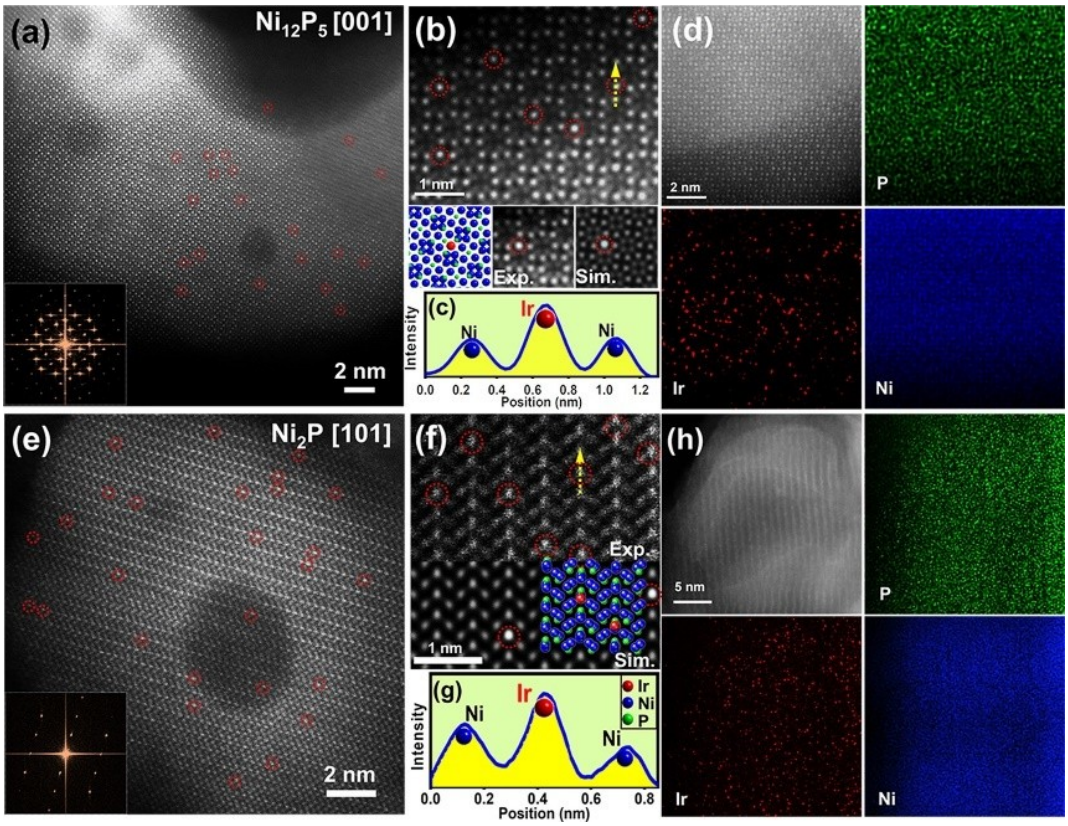

Figure 3. (a) HAADF-STEM image of the SA Ir on $Ni_{12}P_5$ along [001] zone axis, (b) Atomic model and simulation of the HAADF-STEM images of SA Ir is present in place of Ni in SA Ir-$Ni_{12}P_5$, (c) Z-contrast images of the SA Ir-Ni_2P_5 showing SA Ir is embedded in the Ni_2P_5, (d) EDX mapping of IrSA-$Ni_{12}P_5$ showing the homogeneous distribution of SA Ir on $Ni_{12}P_5$; (e) HAADF-STEM image of SAs Ir on Ni_2P along [101] zone axis of SA Ir-Ni_2P and (inset) corresponding fast Fourier transform (FFT); (f) Atomic model and experimental and simulated HAADF-STEM images of SA Ir-Ni_2P; (g) corresponding intensity profile; (h) EDX mapping of IrSA-Ni_2P. Reproduced with permission from ref. [2] Copyright 2021, American Chemical Society

5.3. X-ray Absorption Spectroscopy (XAS)

HAADF-STEM images only provide local information. To find out specifics about SAC's electronic structure and coordination environment, such as how the atoms are distributed, the oxidation state, and how they interact with the support matrix.[33,78,88,92] The local coordination, geometry, and electronic structure of the active sites can be elucidated through XAFS investigations.[78,88] EXAFS and XANES are two common subsets of XAFS. XANES provides information about the electronic configuration, as well as the density of unoccupied states or oxidation states close to the SA's Fermi level.[33] Because of the hybridization effects and many transitions that occur simultaneously, evaluating XANES features is difficult.[92] Three parts make the XANES region: the pre-edge, the edge, and the post-edge. As it originates from the excitation of core electrons to localized unoccupied states, the pre-edge part can reveal insights regarding local symmetry. The geometric arrangement of adjacent ions can be inferred from the pre-edge, and the oxidation state of the species being probed can be determined from the post-edge. Analysis of oxidation states and theoretical modelling are standard practices in XANES interpretation. The EXAFS widens the absorption edge's energy window from 30–50 eV to 1000 eV or more.[20] By using EXAFS, one can determine chemical bonding, the average atomic distance between absorbing and backscattering atoms, and the average coordination number of the surrounding central metal atom.[20,78,79]

Using the Fourier-transformed EXAFS (FT-EXAFS), the radial structure-function (R space) can be used to differentiate between atomic sites that are part of clusters or particles and those that are single.[33,78,79] The coordination of individual atoms can be deduced from FT-EXAFS spectra, which reveal details regarding coordination numbers and interatomic distances.[78] One primary peak in R space is caused by metal coordination with non-metallic elements such as C, N, O, and P, when there is no metal-metal coordination in the SACs.[79] Recent advances in *in situ* XAS analysis have made it possible to elucidate the function of SACs in catalytic processes by providing novel insights into the time-dependent variations in reaction conditions.[16,92] During OER, *in situ* EXAFS is a great tool for understanding the electronic structure of the active sites and the coordinating environment.

The near-edge EXAFS spectra of CoSSPIL/CNT (0.5–1.5) showed an L3 edge in the 775–785 eV range (Figure 4e).[83] The L3 peak occurs as a result of the excitation of Co 2p core electrons ($2p^63d^7$) to vacant 3d orbitals of Co^{II} ($2p^53d^8$). A black vertical line in the CoSSPIL/CNT-0.5 spectra at 777.3 eV appears due to the t_{2g}-holes that are found in an octahedral coordina-

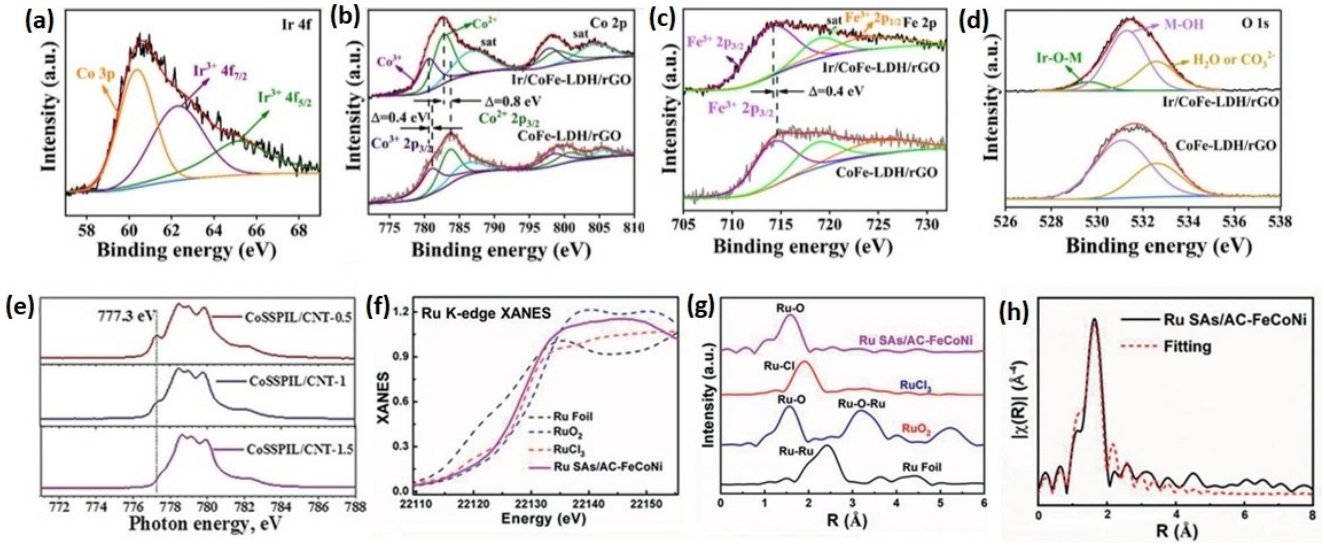

Figure 4. (a) X-ray photoelectron spectroscopy (XPS) of SA Ir-CoFe-LDH/rGO; (b) XPS of the Co 2p of the SA Ir-CoFe-LDH/rGO showing negative shift compared to the CoFe-LDH/rGO due to interaction of the SA Ir with CoFe-LDH/rGO; (c) Similarly, XPS of the Fe 2p of the SA Ir-CoFe-LDH/rGO showing negative shift compared to the CoFe-LDH/rGO after loading of the SA Ir with CoFe-LDH/rGO, (d) XPS of the O 1s of the SA Ir-CoFe-LDH/rGO showing negative shift compared to the CoFe-LDH/rGO due to interaction of the SA Ir with CoFe-LDH/rGO as well as the formation of the Ir–O–M bond. Reproduced with permission from ref. [91] copyright 2023, Wiley.; (e) Near edge X-ray absorption fine structure (NEXAFS) spectra of CoSSPIL/CNT having different amount of cobalt with respect to ligand. Reproduced with permission from ref. [83] copyright Wiley; (f) XANES spectra of RuK-edge showing SA Ru with oxidation state between 2 and 3; (g) R-space Ru K-edge EXAFS spectra showing Ru is present in the form of Ru–O instead of the Ru clusters and $RuCl_3$ residual; (h) EXAFS fitting showed that Ru atom is coordinated with four oxygen atoms. Reproduced with permission from ref. [70]. Copyright 2021, Wiley.

tion environment around Co^{II} ions. As the concentration of the polymeric ionic liquid (PIL) increases, a decrease in the peak corresponding to the 777.3 eV was observed. This is due to a change in the coordination from octahedral to tetrahedral. At high concentrations of the PIL in the CoSSPIL/CNT-1.5, the peak at 777.3 eV disappears due to the three partially filled t_{2g} orbitals in a tetrahedral configuration. Increased ionic liquid (IL) concentration decreases the energy gap (e_g) and splits the Co^{II} ion's t_{2g} orbitals. This causes weak Co-ligand interactions and high-spin states. The process may easily oxidize Co^{II} to a higher valence state (Figure 4e).

From the XANES, the oxidation state of Ru SA on FeCoNi-LDH was found to be 2.8 (Figure 4f).[70] The FT-EXAFS spectrum of the SA Ru on the FeCoNi-LDH showed one prominent peak that was attributed to the Ru–O bond (Figure 4g). Since the SAs R/AC-FeCoNi did not include any Ru–Cl or Ru–Ru metal bonds, neither Ru clusters nor $RuCl_3$ residuals could be detected. These findings demonstrated that AC-FeCoNi sustained the isolated Ru atoms. Furthermore, the R-space fitting of the EXAFS for SA Ru/AC-FeCoNi has shown that each Ru atom was attached to four oxygen atoms (Figure 4h). The wavelet transforms (WT) of Ru K-edge EXAFS oscillations revealed the main peak at ~4.3 $Å^{-1}$ for the Ru–O bond in SA Ru/AC-FeCoNi. (Figure 4h). XANES and EXAFS showed that SA Ru formed a strong interaction with oxygen present in AC-FeCoNi LDH support.

5.4. Fourier-Transformed Infrared Spectroscopy (FTIR)

FTIR is able to discern the existence or non-existence of nanoclusters and nanoparticles through the observation of the sensitive vibration mode of the adsorbed CO molecules on the surface of the SACs.[10,81,93] In situ diffuse reflectance infrared Fourier transform (DRIFT) studies with CO as a probe molecule further support the idea of metal species in atomic dispersion.[93] Zhang et al. used the DRIFT method for the detection of the SAC by using CO as a probe.[31] Two noticeable peaks were seen for C-$Rh_1/Co(OH)_2$ at 2083 and 2010 cm^{-1} due to the symmetric and asymmetric stretching vibrations of CO from the mononuclear $Rh_1(CO)_2$ species, respectively. Similarly, in the case of C-$Pd_1/Co(OH)_2$, a peak at 2132 cm^{-1} is ascribed to top CO adsorption on singly dispersed Pd species.[31] while the peak at 2110 cm^{-1} in C–$Pt/Co(OH)_2$ is attributed to CO that has been linearly adsorbed onto atomic Pt species. For C-$Au_1/Co(OH)_2$, one peak at 2165 cm^{-1} was the most prominent suggesting that the CO was adsorbed with mononuclear Au species.[31]

6. Atomic Site-Support Interaction

The difference in the catalytic activity of SACs with the same atomic sites can be explained by multiple factors. (i) The coordination environment of the atomic sites largely controls its properties. For example, the coordinatively unsaturated metal sites like MO_5 showed far better adsorption of the substrate compared to MO_6 sites. Similarly, the coordination of

the atomic sites can be varied with multiple non-metals like S, P, N, etc., to attain tune properties. (ii) The metal-metal interaction between two atomic sites in a synergistic manner also improves the electrochemical activity. (iii) As mentioned in the introduction part, the electrochemical properties of the active sites of SAs are largely controlled by the support material. The different supports offer a wide variation in the charge distributions around the atomic sites. The interaction between the atomic site and support also controls the electrochemical properties. Therefore, the same atomic site on the same support showed quite different electrochemical properties.[94]

For example, Zeng and co-workers loaded a single atom Ir on an oxygen vacant site (VO) of a defect-rich CoOOH surface and on a three-fold hollow site (TO) of CoOOH and explored the effect of different anchoring sites on OER activity.[95] A superior OER activity of Ir_1 in the vacancy in CoOOH was observed to that in the three-fold hollow site. The spectroscopic and DFT calculations showed that Ir_1 in two anchoring sites activates CoOOH through two different mechanisms. A lower band gap and better electron transfer from SA to CoOOH in Ir_1/TO-CoOOH results in stronger interaction with intermediates than the original CoOOH. However, in Ir_1/VO-CoOOH the single-atom Ir interacts with oxygenated intermediates by configural rather than electronic adsorption adjustment. Hydrogen bonding between the coordinated oxygen of single-atom Ir core and oxygenated intermediates stabilizes them and decreases the energy barrier in the rate-determining step. Due to the difference in the intermediate adsorption in the RDS, Ir_1/VO-CoOOH needs a lower overpotential (i.e., 200 mV) requirement for OER than Ir_1/TO–CoOOH (270 mV). Further, XANES spectra revealed a difference in Ir valence states between Ir_1/TO–CoOOH ($+3$ to $+4$) and Ir_1/VO–CoOOH (slightly higher than $+4$), possibly due to differing anchoring sites.

Among different supports, TM-LDHs were extensively studied to load SAC of noble metals. The adjustability of the layered metal cations, as well as the ratios of M^{II}/M^{III} and anions, yield a vast array of nanoarchitectures with diverse properties. LDH contains OH^-, O^{2-}, or other anions and a large extent of water that adjusts the coordinating sites of single atoms.[66,96] These properties offer unique anchoring sites and chemical bonding models for supporting noble metal atoms such as Au, Ru, and Ir. Further, amorphous LDH contains vacancies that provide diverse coordination environments for the binding of the SAs and stability to the catalyst. LDH also allows the dispersion of SA atoms solely on the substrate surface.[66]

The atomic site of noble metal on LDH supports can offer three distinct features for water oxidation: (i) Solely single atom noble metal as the active site for the substrate binding, (ii) LDH as the active site, and (iii) both offer the active sites. The noble metal supported on the LDH surface can serve as the OER's active site while transition metals LDHs can tune the electronic structure of the atomic site via charge redistribution, further enhancing OER activity. In some cases, single atoms improve the OER activity while M atoms in the MOOH offer the active sites as they adsorb OER intermediates and facilitate the OER. The noble metal atomic sites redistribute the charge around the active sites to improve the intermediate adsorption and hence OER activity. In the case of Ir_1-CoOOH and Au_1-NiFe-LDH, both Co and Fe provide the active sites for OER while Au or Ir-SA modulates the electron density of Co and Fe in LDH, facilitating the adsorption of intermediates O* and OH* and accelerating the reaction kinetics.[49,95]

For the carbon-supported SAC, the precise role of the single sites is easier to realize, considering carbon is the spectator in the OER process. SA bound to different atoms results in different activities that affect the lowest density of states (DOSs) near the Fermi level, affecting the adsorption energy for reaction intermediates during OER. For example, Ni_1 present in different arrangements in Ni@Divacancy, Ni@D5775, and Ni@-perfectly arranged hexagons Ni@POHC showed different OER activities due to difference in the coordination around it.[97]

However, pure carbon tends to dissolve under electrochemical conditions, leading to instability in carbon-supported SAC. Additionally, the simplicity of carbon restricts the diversity of coordination environments and metal-support interactions.[98] High-temperature thermal treatment in an inert environment and doping of the p group element is needed to overcome the demerits, which is not required in the case of the LDH. Further, previous reports showed that LDH with defects serves as a support for SA that can improve the metal support interaction to stabilize SA with high metal loading.[66] In contrast, during high-temperature pyrolysis, there is the possibility of aggregation and coalescence.[58] Hence, pre-and post-treatment is required, which offers extra advantages for LDHs over carbon support. Further high-temperature pyrolysis leads to low loading.

Other transition-metal-based compounds like metal oxide and sulfide have been explored as the support of SA. However, all these materials are converted into MOOH during alkaline OER.[99,100] The Raman spectroscopic characterization of the SA Ir–$CoNiO_2$ after OER showed that phase transition into $M^{3+}OOH$ occurred on the surface of the Ir_{SA}-V_O-$CoNiO_2$.[101] A similar phase transition occurred on the surface in the cases of Ir@IrNiO and Pt_1@NiO.[99,100] In the case of phosphide-based catalyst Ir_{SA}-Ni_2P, the harsh alkaline OER conditions lead to the reconstruction of nickel phosphide and the formation of the Ir–O–P/Ni–O–P bonding environment that modulates the adsorption and desorption of the OER intermediates, boosting OER activity.[2] Similar findings have been made for Ir_{25}–$Fe_{16}Ni_{100}P_{64}$ nanoparticles applied for efficient alkaline OER that also transformed during electrocatalysis. Though already the Ni species on the surface of the Ir_{25}-$Fe_{16}Ni_{100}P_{64}$ nanoparticles before OER testing is oxidized into NiO_x/NiOOH species, after OER testing no metallic bonded phosphide species could be found, only oxidized phosphate in a MO_x/MOOH (M = Fe, Ni) layer.[102] A contemporaneously published study on Ir SA decorated on a one-dimensional (1D) nickel phosphide polymorphic heterostructure (NPPH) led to the same conclusion, where the phosphide species was transformed into a phosphate that promotes the OER.[29]

7. Application of SACs in OER

The support plays a crucial role in SA electrocatalysts by stabilizing and anchoring the individual metal atoms and so affecting the stability, selectivity, and catalytic activity.[17,21,78,103] In order to realize the reaction routes and overcome the kinetic barrier, the synergy between the metal site and the support might become important. To develop a stable SA electrocatalyst, it is crucial to regulate the substrate-metal atomic coordination. Important considerations in this respect include heteroatomic intermediates, coordination numbers, and the density or amount of metal atoms. A successful method is to change the carbon substrate by adding heteroatoms such as N, O, and S, or to pre-coordinate the metal atoms with ligands that include these heteroatoms.[10,18,40,80] This approach ensures the binding and even dispersion of SACs during high-temperature pyrolysis. Similar tactics are observed in utilizing precursors based on MOFs or COFs for the pyrolytic synthesis of SA electrocatalyst. This typically results in M–N–C structures, which are extensively investigated for their electrocatalytic applications. Improving the adsorption/desorption of different intermediates and lowering the energy barriers for the reactions, SAs combined with np's in these cases effectively stimulate the redistribution of charges at the active metal sites.

7.1. SAC@oxide

SA based on noble metals have recently shown improved activity towards OER when combined with transition metal oxides.[101,104,105] It is possible to stabilize SAs on oxide surfaces by taking advantage of the strong metal-oxygen interactions, especially at the coordinatively unsaturated or empty sites. Tuning these interactions can enhance the stability and catalytic activity.

Ir@IrNiO, was synthesized by Liu and colleagues and used for alkaline OER.[99] Ir@IrNiO contained high oxidation states of the SA Ir^{IV}, and surface high-valence states Ni^{III}. Due to the excess loading of SA, extra Ir exists in the form of metallic nanoparticles that bond with and pull surface Ni atom charges and promote the formation of surface Ni^{III}. The XPS, EXAFS, and XANES indicate that Ir@IrNiO has a much lower Ni(II) content than NiO, suggesting that Ir modifies the coordination environment of the Ni atoms and stabilizes the higher Ni^{III} oxidation state. The increase in the fraction of Ni–OH in O 1s XPS confirms that the addition of the Ir promotes surface Ni(III) formation because surface Ni^{III} sites easily adsorb –OH groups compared to Ni(II), thus producing higher Ni–OH proportions in Ir@IrNiO. Further, SA iridium caused the oxygen vacancy in Ir@IrNiO because of Ir^{IV} doping. The higher number of surface available Ni^{III} sites, vacancies, and SA Ir^{IV} are expected to boost the OER performance. This results in a change in the catalyst's intermediate adsorption efficiency. The higher valance Ni^{III} activates the H_2O molecule at low voltage and forms Ni^{III}–*OH. At high bias voltage, the intermediate of Ni^{IV}–$O^{\bullet}$ is formed and transported to the SA Ir^{IV} sites to make Ir^{IV}–O–O and OH^-. Similarly, the formation of a higher oxidation state of Ir^{IV} in Ir-NiO_x serves as an active site and improves NiO's reactivity toward the OER intermediates, enhancing OER activity. The observed phenomenon was attributed to the introduction of excess electrons into NiO by the substituted Ir atoms, attributed to the higher formal charge of Ir (+4) compared to Ni (+2).[105]

An enhancement in the activity has been observed for SA Ir atom-modified oxygen vacant-$CoNiO_2$ support. This modification promotes the lattice oxygen oxidation route for OER.[101] This is an improvement over the present AEM mechanism, which encounters an energy barrier of 3.2 eV between OH* and OOH*. In particular, the $CoNiO_2$ substrate allows for the easy transfer and transformation of lattice oxygen due to the presence of the weak metal-oxygen bond. The addition of Ir atoms in $CoNiO_2$ leads to the considerable overlap of the Ir 5d and O 2p bands, and the formation of the stronger covalent Ir–O bond during the reaction facilitating the transfer from O–O to O–O*. However, oxides usually suffer from poor conductivity and they are not suitable as the support of SAC used for electrocatalytic applications.[18]

In some cases, improving electron transport during OER is achieved by increasing the catalyst's conductivity after adding SAC to the support.[105] SA Ir on NiO_x tuned the number of d electrons around the Fermi level and facilitated their transition into the conduction band to increase the catalyst conductivity.[105] The OER activity of NiO (001) was significantly enhanced by the presence of a single Ir atom, which acts as the active site and boosts the activity of the neighboring Ni atoms towards OER. The electrocatalytic activity of Ir_1 on NiO_x was found to be far better than that of commercially available IrO_2 because of the presence of more number of Ir-species with a 4 + oxidation state. The XANES analysis of SA Ir-NiO indicates a slightly higher oxidation state of Ni compared to NiO after Ir doping. FT-EXAFS reveals an Ir–Ni bond (R > 2 Å) in Ir-NiO instead of Ir–Ir bonding. In FT-EXAFS, the peak at 2.5 Å is caused by Ir–Ni scattering, which means that there are Ir-O–Ni bonds in Ir-NiO, which are different from Ir–Ir bonds. Additional evidence of Ir–Ni scattering paths and EXAFS fitting of Ni further indicate the presence of single Ir atom doping in NiO. Further, the increased Ni oxidation state is supported by the shorter Ni–O distance in Ir–NiO compared to NiO. The higher oxidation states of Ni and Ir, along with the formation of Ir-O–Ni bonds promote the OER activity.

In Pt_1@NiO, active phase γ-NiOOH was formed to improve the electrocatalytic activity.[100] The weakening of the Ni–O bond and an increased charge transfer from Pt to Ni via the O bond improves the OER activity. Despite not serving as an active site for the OER, the DFT analysis showed that atomic SA Pt increases the phase transition rate by lowering the migration barrier of nearby Ni atoms. The primary binding sites in metal oxide supports are predominantly offered by the anionic oxygen species present on their surfaces, notably O^{2-} and OH^-. These species are not very effective at attaching metal atoms; thus, they are not ideal for creating atomically distributed catalysts with a high metal loading.

7.2. SAC@LDH

LDH represent a type of two-dimensional layered material that has been extensively investigated for electrocatalytic OER.[106] In these LDHs, the presence of trivalent metals (M^{III}) alongside divalent metals (M^{II}) occurs due to electrostatic repulsion, resulting in an even distribution.[96] LDHs serve as commonly utilized as support due to their plentiful surface hydroxyl groups and adaptable layered structure, enabling efficient dispersion of the SA.[26,45,107] The SAs metal atoms form a bond with the LDH support through the SA–O–M linkage, establishing a robust electronic connection with the central metal atom and the LDH support.[45,58,107] Additionally, the SAs on the surface can interact with OH^-, O^{2-}, H_2O, or other anions, offering further avenues to adjust the electronic states of these atomic metals. These combined attributes of anchoring SAs onto LDH result in distinctive and exceptional performance during catalytic reactions.[45,49,58] However, low conductivity is a major issue that hinders the use of the LDH for the OER. Several methods have been developed to enhance LDH catalytic activity via controlling morphology, defect development, charge transfer, etc.[108] The introduction of SACs promotes the electron and mass transfer during the OER and hence improves the overpotential.[26] Even the introduction of the SAs on LDH can create structural defects like cationic or oxygen vacancies. Cationic defects can also serve as the binding sites of SACs.[26,45,107] As a result, a reduction in the required overpotential for OER is observed.

The formation of the vacancy provides diverse coordination environments site for the binding of the SAs and provides stability to the catalyst. Compared to NiFe LDH, the OER activity was increased by a factor of 6 by SA Au supported on NiFe LDH.[49] The improvement in the activity is due to the formation of the NiFeOOH during the OER. The fact that OER activity can be improved by dispersing a SA Au on a NiFe-LDH catalyst is due to the formation of interface sites between the SA Au and the NiFe-LDH. The single Au atoms adjust the charge distribution via electron transfer at the Fe active site, ultimately improving OER performance. The Density functional theory (DFT) calculations with the Hubbard-U method provide an insightful view to reveal the function of single Au atoms. Single Au atoms reduced the adsorption energies of O* and OOH* intermediates for Ni–Fe LDH. The theoretical results showed that the LDH substrate and interlayer CO_3^{2-} anions in Au_1/NiFeOOH-NiFe LDH maintain the charge balance of oxyhydroxide, stabilize the surface NiFeOOH layer, and optimize OER intermediate adsorption energies on Fe active sites.

Similarly, the single Ir atoms adjust the charge distribution via electron transfer to the Co active site in CoOOH, ultimately improving OER performance.[95] The DFT calculation indicated that Ir single atoms did not provide an active site during OER. Instead, Co atoms were identified as the actual active sites, as they adsorbed OER intermediates and participated in OER. Furthermore, the redistribution of charge around the active Co atoms, along with their neighboring Ir atoms, influenced the electronic structure of Co. This modulation facilitated the adsorption of intermediates and accelerated the reaction kinetics.

Analysis of charge density difference in Ru_1/NiFe-LDH and NiFe-LDH revealed that Ru atoms primarily donated electrons to neighboring O atoms and bridging Ni and Fe atoms through Ru–O–Ni, and Ru–O–Fe bonds.[45] This suggests that electron transfer in the Ru_1-NiFe LDH predominantly occurs from Ru to O and then Ni, and Fe atoms. The presence of SA Ru initiates electron rearrangement and fosters synergistic electronic interaction between SA Ru and NiFe LDH. Consequently, SA Ru facilitates the optimization of the binding energy between Ru_1-NiFe LDH and OER intermediates. In the case of Ru_1-CoCrLDH, the density of the d site of Co showed that the SA Ru atom modulated the electronic properties of Co to facilitate the adsorption of reaction intermediates to an optimal level.[45] In a very similar approach, SA Ru was loaded onto NiFe-LDH through an oxygen-coordinated bond using a solution reduction procedure.[45] The SA Ru/NiFe-LDH shows greater activity (196 mV at 10 mA cm^{-2}) than pure NiFe-LDH (316 mV) and possesses 99.3% of Faradaic efficiency due to the cooperative effect.[45] The initiation of OER in SA Ru/NiFe-LDH may be triggered by the existence of ruthenium (Ru) species, potentially enhanced by spatial electron rearrangement. DFT showed this process effectively lowers the energy barrier of the RDS ($*O + OH^- \rightarrow *OOH + e^-$). Similarly, the presence of Ru–O moieties in Ru/NiFe-LDH boosts the O–O coupling, which increases the OER kinetic rate, as seen with SA Ru on defective NiFe LDH (189 and 220 mV @10 and 100 mA cm^{-2}), as compared to NiFe LDH (250 and 290 mV) and IrO_2 (350 mV).[66]

Earlier it was shown that the introduction of the SA Ru atom on the CoFe-LDH leads to an improvement in the conductivity of the CoFe-LDHs due to the band gap reduction.[26] The high synergistic electron coupling between the SA Ru and the LDH allows SA Ru to transfer electrons and modify the charge distribution. Changing the adsorption energies of O* and OOH* intermediates and encouraging the adsorption of OH^- improves the OER performance of the SA Ru-CoFe-LDH by lowering the overpotential in the rate-limiting step from O* to OOH. The SA Ru on the CoFe-LDHs produced high OER performance (198 mV cm^{-2}@ 10 mA cm^{-2}) with a low Tafel slope of 39 mV dec^{-1} compared to the CoFe-LDH.[26] Also, it was found that the durability of the CoFe-LDH was improved upon the introduction of the SA Ru compared to the CoFe-LDHs and commercial RuO_2 catalysts due to the formation of the Ru–O–M bond. At a potential of 1.6 V, the bond lengths of different metal-oxygen bonds like Co–O, Fe–O, Co–O–Fe, Co–O–Co, Fe–O–Co Co–O–Ru, and Fe-O–Ru shorten irreversibly, fixing and preventing the disintegration of Ru during OER as a result, the stability of the catalyst was increased. The computational study also showed that the electron cloud density of Co and Fe atoms in Ru/CoFe-LDHs was lower compared to CoFe-LDHs. This suggests that the addition of Ru could diminish the electron cloud density of Co and Fe, which is crucial for the OER process.[26]

The same conclusion holds for Ru SAs; when loaded on hybrid amorphous/crystalline FeCoNi-LDH, the catalyst needs a very low overpotential of 205 mV at 10 mA cm^{-2}.[91] According to the DFT investigation, the hybrid amorphous/crystalline

FeCoNi-LDH stabilizes individual Ru atoms, which speeds up the OER process by promoting the production of Ru–O*. The unsaturated coordination sites and defect sites in the amorphous outer layer of Ru SAs/AC–FeCoNi anchor individual Ru atoms. The crystalline inner layer possesses a highly symmetric rigid structure, improving the stability of the support for enduring OER performance.

The leaching of the Fe from the Fe-based LDH hugely impacts the long-term durability of the catalyst.[109] Cao et al. used SA Ir on the CoFe-LDH/rGO for the electrocatalytic OER in an alkaline medium.[91] As an active site for OER, the SA Ir-doped CoFe-LDH/rGO prevents Fe dissolution in long-term durability tests. The activation-induced increases in the dissolution rates of Fe and Co are significantly larger than those of Ir, suggesting that these elements are not the primary drivers of the OER process in SA Ir/CoFe-LDH/rGO. Instead, the exceptional OER performance is mainly due to the doped Ir atoms. The peak of the Co(II)/Co(III) and Fe(III) shifted to the negative after the Ir doping on CoFe-LDH/rGO. The establishment of the Ir–M–O link and the strong interaction between Ir and Co/Fe on CoFe-LDH/rGO are the causes of the negative shift. The SA Ir/CoFe-LDH/rGO exhibits far higher OER activity than CoFe-LDH and CoFe-LDH/rGO, all while requiring a much lower overpotential of only 195 mV to generate current densities of 10 mA cm^{-2}. At a current density of 200 mV cm^{-2}, the SA Ir/CoFe-LDH/rGO exhibits excellent durability in an alkaline solution for over 400 hours.

The coordination environment of the atomic sites plays a crucial role in modulating its electronic structure, interaction with the support, and hence its activity and stability in the electrochemical process. However, the variation in the coordination environment of the atomic sites used for the OER is limited compared to the other electrocatalysts. In OER catalysts, mostly MO_6/MO_5 coordination was observed as, in most cases, the single atomic sites are supported on metal oxide or hydroxide.

The change in the local coordination environments in NiV-LDH has been observed due to the introduction of SA Ir.[110] A severely deformed octahedral V–Ni/V environment is implied by the subtle effects of the Debye-Waller factor (σ^2) on the catalyst's local coordination environments. This shift in the local coordination parameters impacts the RDS. The V K-edge XANES analysis of NiVIr-LDH exhibited a notably enhanced pre-edge peak compared to NiV-LDH. This observation indicates a substantial distortion of the octahedral geometry of the V sites due to the presence of SA Ir in NiVIr-LDH. Introducing Ir into NiV-LDH enhances conductivity in the M–OH and M–O processes, leading to improved OER performance owing to lattice distortion and vacancies. At the optimal weight percentage of SA Ir, NiV-LDH demonstrated an overpotential of 180 mV, achieving a current density of 10 mA cm^{-2}, outperforming NiV-LDH (Figure 5a). Both theoretical and experimental investigations corroborated the idea that Ir doping lowered the energy barrier and sped up OER. (Figure 5b–c).[110]

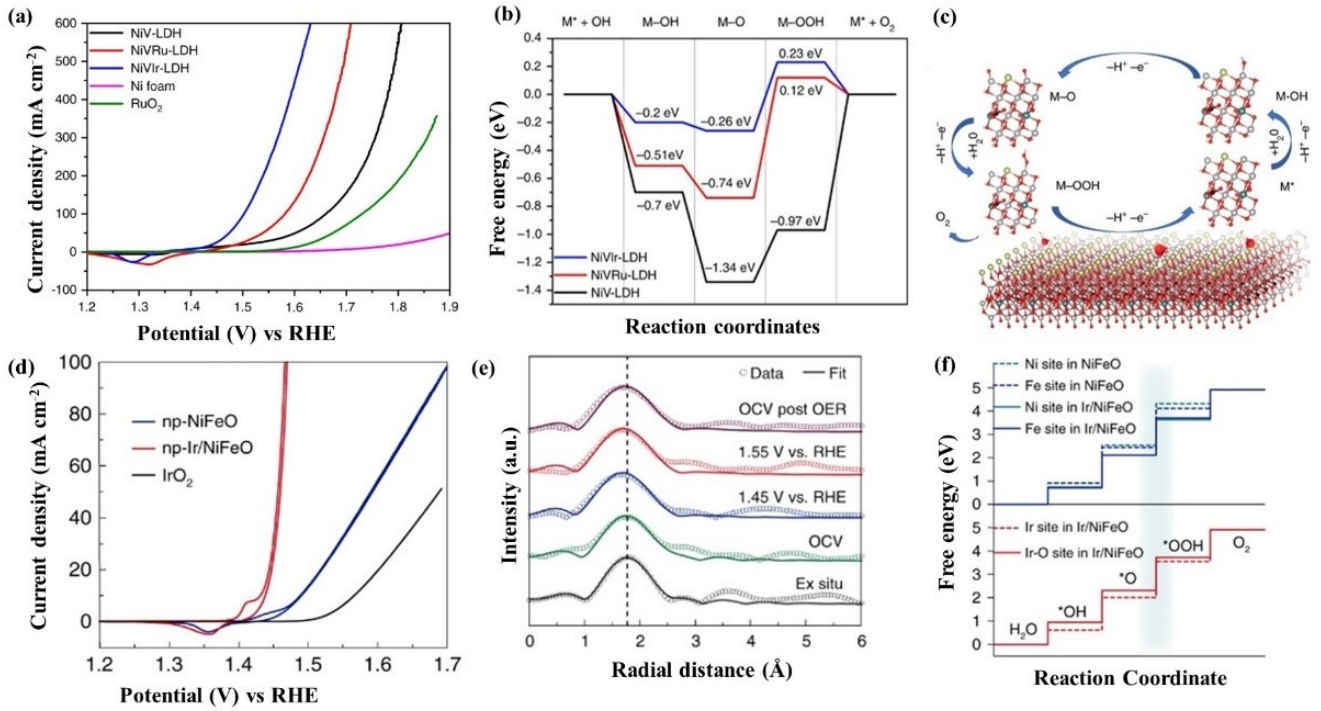

Figure 5. (a) Linear Sweep Voltammetry profile showing an improvement in the OER activity for SA Ir on NiV-LDH compared to the Ru on NiV-, NiV-LDH and Ru_2O in 1 M KOH solution; (b) The free energy diagram of SA Ir NiV-LDH, Ru on NiV-LDH and NiV-LDH showing in a decrease in free energy for OER is more in SA Ir NiV-LDH than Ru on NiV-LDH and NiV-LDH; (c) The atomic model for OER by SA Ir NiV-LDH. Reproduced with permission from ref. [110] copyright 2019 Springer Nature

Incorporating SA Ru into CoCr LDHs improves the charge transfer between Ru, Cr, and Co, which in turn decreases the adsorption of O* and OH* at the Co sites of CoCrRu LDHs, leading to increased OER activity.[111a] By increasing electron donation from Cr to different oxygenates, the SA Ru dopants in CoCr LDHs can reduce the Co d states, breaking the scaling connection and facilitating the higher activity

The enhancement of water oxidation activity was demonstrated in the previous work by incorporating higher valence transition metal ions, such as M^{IV}/M^{V}, into metal oxides and hydroxides.[41,105,112,113] These ions were produced through a potential-dependent deprotonation reaction. The higher oxidation state of a SA iridium was loaded on the NiFeOOH support by an *in situ* cryogenic-photochemical reduction technique by Zheng et al.[112] The DFT calculations have revealed that the NiFeOOH layers have been covered by IrO_6 octahedral SAC. The *in situ*-operando Ir L3-edge XAS results show that the NiFeOOH undergoes a high degree of oxidation (+ 5.3) during OER, which is in agreement with the predictions of DFT and spectroscopic measurement. The highly oxidized Ir single-site shows superior OER performance with an overpotential of 183 mV at 10 mA cm^{-2}.[112]

7.3. SAC@phospide

The d-band structure of the transition metal can be altered by phosphorus alloying, which improves catalytic activity.[114] Under OER conditions, they self-reconstruct their surfaces to produce oxyhydroxides, which provide an abundance of oxygen ligands for the attachment of SAs.[2,28] Ir SAs were deposited on the NiFeP and used for electrocatalytic OER in the alkaline medium.[28] The Ir-NiFeP after electrochemical activation, led to the formation of the stable isolated Ir atoms with higher valence due to the presence of more oxygen ligands in NiFeOOH from Ni_2P after the activation process. The SA Ir atoms can improve the formation of NiFeOOH, triggering the intrinsic activity of these oxyhydroxides and consequently expediting the reactions. The np-Ir/NiFeO catalyst demonstrates exceptional electrochemically OER activity, displaying a significantly low overpotential of 197 mV. This achievement surpasses the commercial IrO_2 by 131 times and exceeds the activity of the majority of previously reported catalysts. In order to achieve their exceptional catalytic efficiency, isolated Ir atoms go through a deprotonation process during the OER, which was shown by XAS and DFT simulations. This process changes their active sites from one to multiple active sites. This study underscores the significance of discerning the detailed structure of the components formed during reconstruction and advances our comprehension of how SACs dynamically influence electrocatalytic OER activity.

The PCET process during OER may be improved by the formation of Ni–O–P bonds at the surface of the catalyst.[29] To achieve its exceptional OER performance, NPPH–O's ((NPPH is a mixed phase of Ni_2P5 and Ni_2P) polymorphic heterostructure probably works in tandem to optimize the valence electron state of active sites and the adsorption energy of intermediate molecules. Similarly, the introduction of the Ir SAs at Ni_2P lead to improvement in the current density at 1.53 V vs RHE which is 28 times higher than the current density of the IrO_2.[2] The Ir-SA-Ni_2P catalyst could require an overpotential of 149 mV to attain 10 mA cm^{-2}OER current density. The improvement in the activity was due to the preferentially occupied Ir SAs Ni locations on the surface Ni_2P. Reconstruction of nickel phosphide leads to the formation of the Ir-O–P/Ni-O–P bonding environment that modulates the adsorption and desorption of the intermediates, boosting OER activity. The Ni K-edge XANES spectra of both SA–Ir–Ni_2P and Ni_2P exhibited pre-edge and white line peaks at ~8333 eV and 8350 eV, respectively (Figure 6a).[2] The introduction of Ir in Ni_2P resulted in a noticeable change in the valence state of Ni, indicating a modulation in the electronic structure of Ni_2P (Figure 6a). Furthermore, with the introduction of Ir, the pre-edge peak in the Ni K-edge became more intense, indicating a potential distortion in the octahedral coordination of the Ni. (Figure 6a). The XANES spectra of the Ir L_3-edge of the SA Ir-Ni_2P showed that Iridium was present in a 4+ oxidation state implying an Ir–O–P bond (Figure 6b). FT-EXAF analysis further revealed changes in the bond length of the nickel phosphide bond upon the addition of the Ir, indicating alterations in the Ni geometry (Figure 6c). The peak at 2.25 Å in FT k^3 $\chi(k)$ of Iridium was attributed to the scattering between Ir and P (Ir–P) first shell, indicating the formation of strong bonds with Ni_2P (Figure 6d). The observations presented above provide evidence that SA Ir-Ni_2P particles can form an oxidized surface, characterized by the dominance of Ir–O–P and Ni-O–P bonding at this surface.

The addition of Ir atoms on the NPPH surface also affected the electronic properties of NPPH. This alteration is evident from the missing characteristic Ni–P peak in pure NPPH, which is attributed to the development of a Ni–O–P surface oxidation layer.[29] Furthermore, an increase in the binding energy of the Ni peaks suggests that the Ni atoms on the Ir/NPPH surface are in a higher oxidation state. An increase in OER activity may result from a cooperative change in the valence electron state of active sites and the adsorption energy of intermediate species brought about by the creation of the NPPH–O polymorphism heterostructure. Meanwhile, the annealed Au@Ni_2P sample with the single Au atoms and microscopic Au clusters on Ni_2P demonstrated exceptional OER performance.[63] The OER performance of the annealed Au-Ni_2P sample was significantly enhanced, outperforming a commercial IrO_2 sample by a factor of 16 and a fresh yolk shell by a factor of 12. Moreover, incorporating Au SAs into the Ni_2P alloy phase might alter the electronic structure, further contributing to the enhancement observed in the OER activity. The synergistic impact between the Ni_2P support and the individual Au atoms is thought to be the source of the enhanced activity, which is credited to the active sites. Another potential advantage to the OER is an altered electronic structure that might emerge from the Au SA-doped Ni_2P alloy phase.

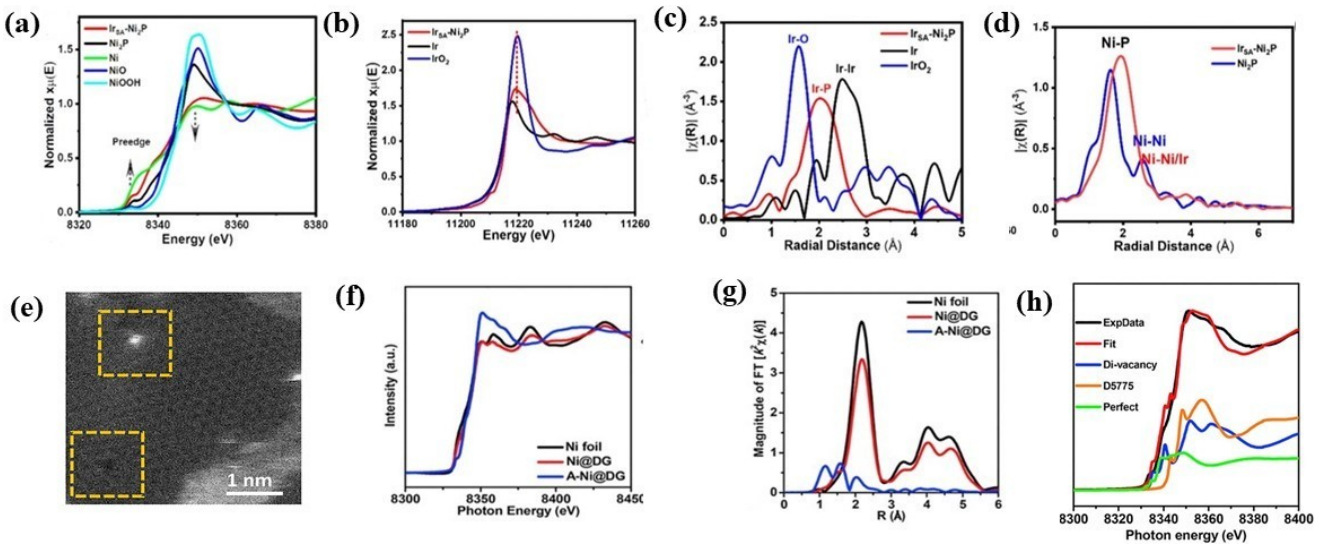

Figure 6. (a) The Ni K-edge of the Ir-Ni_2P shows the distortion of the octahedral coordination of $N_{i2}P$ after loading of SA Ir due to the interaction of the SA Ir with Ni2P, (b) Ir L3-edge XANES spectra of IrSA-Ni_2P. FT- EXAFS spectra of Ni K-edge of Ir–Ni_2P; (c) Ir L3-edge of the IrSA-Ni_2P catalyst and the references; (d) Ir L_3-edge XANES data of SA Ir–NiO, Ir foil, and IrO_2 showing the existence of the higher oxidation state of the SA Ir in SA Ir–Ni_2P. All data indicates the existence of the Ir–O–P/Ni–O–P between Ni_2P support and SA Ir; Reproduced with permission from ref. [2] copyright 2021 American Chemical Society. (e) HADDF-STEM image of A–Ni@DG showing interaction of the SA with defect in carbon support, (f) Ni K-edge XANES spectra of the Ni@DG, A–Ni@DG, and the Ni foil reference samples; (g) K2-weighted FT spectra of Ni@DG, A–Ni@DG, and the reference samples of Ni foil, (h) The LCF of XANES involves theoretical modeling. The red line represents the composite of theoretical model simulations for the three configurations, closely matching the experimental result; Reproduced with permission from ref. [97] copyright 2018, Elsevier

7.4. SAC@metal Hydroxide

The OER activity was found to be improved when $Ni(OH)_2$ was loaded with single W atoms.[64] The low spin W^{VI} (d^0) facilitates the formation of O radicals and O–O coupling at the location where the SA W atom is located. Increased carrier migration from the catalyst to the solution and improved intrinsic catalytic activity are both brought about by W doping in $Ni(OH)_2$. To enhance the OER activity, Zhang et al. introduced SA Ir on the defect-rich cobalt hydroxides ($Co(OH)_2$).[111b] Co–Ir species could develop easily due to the so many active sites offered by the atomically distributed Ir species. At an optimum concentration of Ir, $Co(OH)_2$ showed a better overpotential of 235 mV at 10 mA $cm^{-2,}$ which was better than other concentrations and IrO_2 (280 mV). During electrocatalytic OER, it was found that SA Ir oxidized to a higher valence state (Ir^{IV}) while maintaining atomic dispersion, suggesting that the oxidation process occurred electrochemically. Similarly, α-$Co(OH)_2$ was transformed into unsaturated cobalt(oxy) hydroxide. Accelerating the OER process was due to the cooperative effect of the high-valence SA Ir and unsaturated Co sites, which help in the adsorption of different reaction intermediates during OER.

Similarly, an enhancement in the OER performance has been seen for high valance SA Ir on the Ni vacancies in β-$Ni(OH)_2$ nanosheets.[68] The high valent Ir sites lowered the overpotential by increasing high mass activity. Also, its ability to tolerate the high anodic potential in the alkaline medium during electrochemical transformation increased the catalyst stability. Results from theoretical calculations showed that the RDS process was the deprotonation of adsorbed OH, and it was also explained why high-valence Ir can activate SAs and promote oxygen production.

7.5. SAC@N-Doped Carbon

Recently, greater activity toward OER has been shown by SACs based on noble metals like Ir and Ru with 3d transition metal oxide-based networks.[105] However, a more critical concern regarding the durability of water electrolyzers lies in the instability of OER electrocatalysts when subjected to high overpotential conditions, typically exceeding 1.6 V vs. RHE, in an alkaline medium. SACs are typically found in a scattered form on conductive carbon-based substrates, where they are typically stabilized through the coordination with N or other heteroatoms.[18,20] Due to their superior adsorption characteristics and stability, the nonprecious elements with covalently coordinated transition metal centers show the most promise for electrocatalytic applications. The coordination environment around the SAC largely determines the inherent OER activity of isolated catalytic sites, so it is important to take this into account when designing high-activity SAC for OER.[8] The coordination environment around the SAC tunes the binding energy of metal-oxygen bonds within the different intermediates like M–O, M–OH, and M–OOH during the electrocatalytic OER.[115–117] The manipulation of the electronic properties of the support enhances the OER activity and stability of SACs.

SA Ni supported on graphene shed light on how coordination atoms influence OER activity and stability.[97] Different coordination environments and coordination numbers modu-

late the electronic environment around the SA, which affects the OER activity. To demonstrate the impact of coordination number on OER activity, Zhang et al. anchored atomic Ni on defective graphene with different coordination viz., Ni@Divacancy, Ni@D5775, and Ni@perfectly arranged hexagons (Ni@POHC).[97] Among them, SA Ni@Divacancy showed high OER activity (270 mV at 10 mA cm^{-2}), better than Ni@D5775, and Ni at ordered hexagons carbon as well as Ir@C (320 mV). The high OER activity of the presence of Ni@Divacancy has been associated with the lowest density of states (DOSs) near the Fermi level, providing favorable adsorption energy for reaction intermediates during OER.

Diverse coordination around SAs significantly impact OER activity by influencing their efficiency toward intermediates.[97] According to the XANES curves analyzed using least-squares curve fitting (LCF), there are three different arrangements of atomic Ni on defective graphene (DG). These catalysts exhibit variations in energy-level splits and the DOS of 3d-orbitals of Ni due to differences in carbon coordination. The d-band of the support significantly interacts with the adsorbate's highest occupied and lowest unoccupied molecular orbitals. The strong interaction between the substrate and adsorbates is shown by the significantly larger DOS near the Fermi level.

The HADDF-STEM image of A–Ni@DG indicates the presence of Ni in Ni–C_4 form (Figure 6e). This finding was further confirmed by the XANES spectra of the Ni K-edge (Figure 6f). Notably, the white-line prominent peak of A–Ni@DG appeared higher than that of Ni@DG, indicating an oxidized electronic structure of Ni. Analysis using FT-EXAFS revealed differences in the R space between A–Ni@DG and Ni@DG (Figure 6g). While the EXAFS curve of Ni@DG displayed a dominant peak at 2.2 Å, corresponding to Ni–Ni coordination, A–Ni@DG exhibited three peaks at 1.2, 1.6, and 2.0 Å, indicative of different Ni–C coordination. One peak at 2.2 Å was seen in the EXAFS curve of Ni@DG, which corresponds to Ni–Ni coordination; in contrast, A–Ni@DG showed three peaks at 1.2, 1.6, and 2.0 Å, which point to distinct Ni–C coordination. Moreover, according to the LCF XANES analysis, the XANES data of A–Ni@DG were well-aligned with the superposition of curve intensities of Ni anchored on Di-vacancy, D5775, and perfect hexagons, with a ratio of 36 : 44 : 20 (Figure 6h). This result highlights the reasonable coexistence of the three Ni–C coordination states.

Previous studies have reported that graphene/carbon-based supports exhibit chemical inactivity towards OER.[33,40,115] An improvement has been attained in enhancing the OER performance of SACs, including the adjustment of metal center coordination environments and the interaction of diatomic metal sites.[8] The optimum binding energy for the reaction intermediates during OER is achieved by decreasing the activation energy through doping the carbon support with non-metal elements like C, N, O, and P, as demonstrated in the previous report.[90,116] The introduction of the heteroatom in the coordination forms a strong interaction with the vacant d orbital of the transition metal atom that prevents agglomeration and provides more number active sites during the reaction.[118]

The presence of coordinating O and N atoms modified the SA Ni with different coordination. Compared to the Ni–N–G, Ni–O–G showed improved OER performance in the alkaline media.[116] The difference in the activity was due to more available valence electrons in the Ni–O–G to react with O-atoms of the different intermediate compared to the Ni–N–G, which reduced the energy barrier for the formation of *O during OER. Therefore, Ni–N–G required an overpotential of 224 mV to reach the current density of 10 mA cm^{-2} and showed long-term stability without significant degradation for 50 h at a high current of 115 mA cm^{-2}.

Su et al. synthesized SA cobalt with pyridinic- and amino-N coordination (HNC–Co).[119] The formation of O* intermediates during OER is attributed to the creation of H_2N–(*O–Co)–N_4, validating the four-step mechanism of OER. An increased DOS close to the Fermi level was observed that resulted in the hetero-N–Co bonding to strengthen the 2p–3d hybridization between surface oxo-species and Co active centers. As a result, in HNC–Co, a decrease in the adsorption energy of H_2O (0.5 eV) was observed compared to pure carbon paper, thereby reducing the energy barrier to 0.36 eV for the formation of *O in the RDS.

The d-orbital configurations of transition metals, and more especially the number of d electrons in a metal, have a major impact on OER activity and the mechanisms involved. The effect of the d electron on the OER mechanism was explored with SA Co, Ni, and Fe-NHGFs (N-doped holey graphene framework) in an alkaline medium.[47] For the Co and Fe-NHGFs, OER proceeds via the single-site mechanism on the fact that all OER intermediates bind more firmly at the Fe or Co site than at the C site. Ni-NHGFs follow a dual-site mechanism in which the O* and OH* intermediates are adsorbed on C sites while the OOH* prefers Ni atoms. Due to this, the energy barrier of O_2* desorption was also lowest for the Ni-NHGF compared to the Co and Fe-NHFG due to doping-induced charge redistribution.[47]

7.6. SA@metal Chalcogenide

The metal selenide possesses good metallic properties, optimum eg electronic configuration, and efficient charge transfer, making it the proper choice for electrocatalytic activity. Lei et al. employed the electrochemical method to synthesize high-surface-distributed SA Ir on $Ni_{(3-x)}Fe_xS_2$ (Ir_1/NFS) nanosheets.[62] Due to separate substrate construction and Ir SA deposition, this method allows the dispersion of Ir atoms solely on the substrate surface, not inside the electrode. The DFT studies demonstrated that the formation of the Ir–S–Ni/Fe bond accelerates the formation of the *OOH from an *O group. Furthermore, the projected density of states (PDOS) outcomes reveal that electrons on Ir atoms within Ir_1/NFS reside nearer to the Fermi level and are distributed across the reaction, contributing to improved electrochemical performance through enhanced electron transfer.[75] As a result, Ir_1/NFS exhibits an exceptionally high turnover frequency (TOF) of 9.85 s^{-1} at an

overpotential of 300 mV and a remarkably low overpotential of around 170 mV at a current density of 10 mA cm^{-2}.

It was found that ferromagnetic SA cobalt on the metallic TaS_2 showed an improvement in the OER activity due to the modulation of the spin activity of the Co SA.[120] The experimental investigation demonstrated that a SA situated in the hollow site serves as an active site for the OER, attributed to the presence of spin-polarized electronic states. By adjusting the Co loading, the exchange interactions with neighboring Co sites regulate their spin densities, thereby influencing the OER activity. The presence of neighboring CoTa enhances the OER activity by elevating the spin density of the CoHS active site to an optimal level. This study underscores the efficient modulation of OER performance by optimizing the spin density of SA active sites. It suggests that spin density can function as an activity descriptor in guiding the development of effective magnetic catalysts.

A reduction in the overpotential requirement is observed in the case of Ir loading on the $Co_{0.8}Fe_{0.2}Se_2$.[31] The SA Ir-loaded $Co_{0.8}Fe_{0.2}Se_2$ (230 mV to reach 10 mA cm^{-2}) required an overpotential of 135 mV lower than Ir in an alkaline medium. The strong metal-support interaction and highly efficient charge transfer capability of the support led to an increase in the OER activity of Ir SAs on $Co_{0.8}Fe_{0.2}Se_2$.[31]

The addition of a SA Pt can significantly boost the OER efficiency of $CoSe_2$.[30] The improvement in the activity was explained by the change in the electronic distribution due to the presence of Pt–Co–Se moiety. Pt L3-edge EXAFS revealed that the lone Pt primarily forms an atomic Pt–Co bond at selenium vacancies of $CoSe_2$, generating atomically coordinated Pt–Co–Se arrangements. Additionally, introducing SAs Ni and Ru onto $CoSe_{2-x}$ yields lower OER performance compared to $CoSe_{2-x}$-Pt, possibly due to their lesser degree of electronic distribution asymmetry. The XANES spectra of $CoSe_{2-x}$-Pt at the Pt L3-edge suggest partial oxidation of Pt atoms, with the white-line peak intensity falling between Pt foil and PtO_2. EXAFS analysis reveals Pt atoms predominantly exist as individual species on $CoSe_{2-x}$-Pt, forming Pt–Co couplings at selenium vacancies on the $CoSe_2$ surface. HAADF-HRTEM imaging confirms uniform dispersion of Pt atoms across the $CoSe_2$ basal plane, with FFT analysis identifying the observed plane as the (210) plane of $CoSe_2$. The ordered distribution of Pt atoms, approximately 0.2 nm in size, on Co atop sites is evident in colored HAADF images, indicating successful entrapment of single Pt atoms by selenium vacancies and contributing to enhanced OER activity.

The local density of states (LDOS) of the materials may be affected by the varying degrees of electronic distribution asymmetry. The LDOS around the Fermi level is significantly higher for the 3d-orbitals of Co atoms and the 2p-orbitals of Se atoms in $CoSe_{2-x}$-Pt compared to $CoSe_2$-original and $CoSe_{2-x}$. According to the d-band center theory, heightened electron densities near the Fermi level facilitate the adsorption of adsorbates, with substantial interaction occurring between the substrate's d-band and the highest occupied and lowest empty molecular orbitals of the adsorbate. Similarly, a single Au atom on $CoSe_2$ nanobelts (Au_1-$CoSe_2$) improved the exposure of Co active sites.[121] Consequently, lowering the H_2O adsorption energy on Co active sites was observed to lower the activation energy of the RDS. Due to this, Au_1-$CoSe_2$ nanobelts showed an improvement in the OER activity (303 mV) that is lower than pristine $CoSe_2$ nanobelts (21.1 times), Au np-deposited $CoSe_2$ nanobelts (5.1 times), and the commercial Ir/C (1.9 times), respectively.

7.7. Other Supports

The electrocatalytic OER investigated the SA cobalt-bridged ionic liquid (IL) polymer with an emphasis on the ionic liquid's impact on the t_{2g} configuration.[83] The octahedral Co^{II} geometry is changed to the tetrahedral one, with three t_{2g} orbitals, at an optimal IL concentration. This causes the Co^{II} to enter high-spin states through the formation of weak Co-ligand linkages.

The synergistic interaction between SAs and the support is crucial for stability and high activity toward OER, as shown by the IrNiFe/Ni NW@NanoSheets.[122] Adding the SAs Ir in NiFe/Ni NW@NSs enhanced NiFe/Ni NW@NS intrinsic activity and stability. After 12 hours of CA in a 1.0 M KOH electrolyte, the operating potential of NiFeIr0.03/Ni NW@NSs hardly changed from 10 mA cm^{-2} compared to the NiFe/Ni NW@NSs and RuO_2, indicating that the synergistic effect between Ir SAs and the support may have contributed to the improved stability. One possible explanation for NiFeIrx/Ni's superior performance is that its Gibbs free energy for the oxidation of O* to OOH* is lower than that of NiFe. Ru SACs showed similar catalytic performance to that of Ir SACs.

8. Stability of SACs under OER Conditions

Bridging homogeneous with heterogeneous catalysis SACs present an advantageous approach for optimizing catalytic activity while minimizing the use of metals in chemical reactions.[123] Stabilizing SAs on various support materials, including carbon materials, alloys, metals, and metal oxides/(oxy)hydroxides, etc. has proven to be an effective strategy to significantly enhance OER activity. While, most of the heterogeneous catalysts inevitably transform during OER by self-reconstruction, oxidation, dissolution, and degradation due to electro-derived structural oxidation processes, similar processes are also anticipated in the case of SACs.[124] However, many studies lack stability analysis by *post operando* analysis or rely solely on DFT calculations and especially *in situ* or *operando* techniques to reveal the nature of the real active species in SACs remain scarce.[30,112] Usually, the main focus is given to the synthesis of SACs, facing up to the challenge of maintaining SA active sites, without the active species migrating and aggregating into nanoclusters, and various strategies have been developed to attain an atomically dispersed species.[125] Therefore, stabilizing SACs in the harsh conditions of OER and enhancing their activity remains a challenge. *In situ* analysis is therefore the most important tool to shed light on the functional role of SACs in the OER process and to understand

the reaction mechanism with time-dependent resolution and observe the change of electronic and geometric structure, of the active sites on atomic scale.[92,126]

As described by Yao et al., the Ru–N–C electrocatalyst, consisting of atomically scattered Ru_1-N_4 sites on nitrogen-carbon support, is stable even after prolonged OER. Ex situ TEM, XRD, and XAFS studies confirmed that the morphology and structure were almost identical after the long-time electrolysis, and only a small amount of Ru (5% dissolution) was discovered during the 30-hour OER operation. *In situ* EXAFS and FTIR confirmed the retention of the Ru_1-N_4 moieties in the structure and identified the formation of O–Ru_1–N_4 in *operando* conditions demonstrated to be crucial to form the OOH* intermediate while maintaining an oxidation state between +3 and +4 as further confirmed by DFT.[127]

Following a similar approach, Feng, Liu, and Sun reported a SA site Ru and in this case, it was decorated on CoFe-LDHs (Ru/CoFe-LDHs) that displayed impressive performances in alkaline media exhibiting no loss in activity over 24 h prolonged OER testing. In the analyzed media, they could find no apparent Ru loss from the structure into the electrolyte, and *ex situ* TEM and XPS revealed no apparent change of the catalytic active species after long-term OER in comparison to the as-prepared one. The *in situ* XANES and EXAFS revealed the redox reversibility of Ru and irreversibility of Fe and Co, suggesting that Ru is the real active site in Ru/CoFe-LDHs but Co and Fe interaction anchor Ru tightly to prevent dissolution and improve activity and stability.[26]

A Year later. Wu and Li et al. prepared atomically dispersed Ru on a FeCoNi-LDH (Ru SAs/AC-FeCoNi) and could not see structural changes via XRD and TEM (Figure 7). But via *operando* Fe K-edge, Co K-edge, Ni K-edge, and Ru K-edge XAS, with increasing potential from open circuit voltage (OCV), they observed an irreversible oxidation of Fe, Co, and Ni. The shifting of the Ru XANES edge to lower energy indicated a reversible change of Ru valence between +3 and +4 during OER, which was also supported by XPS data. Further, they observed

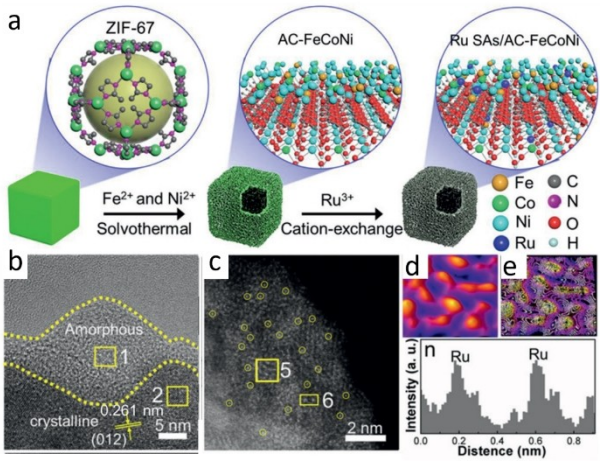

Figure 7. (a) The synthetic scheme of Ru SAs/AC-FeCoNi. (b) HRTEM images of Ru SAs/AC-FeCoNi and (c) AC HAADF-STEM images with 3D AOGF mapping (d) and (e) the 3D isolines and intensity profile for the area 6 in figure (c), modified with permission from ref. [70] copyright 2019, Wiley-VCH.

reversible structural changes shown in the Ru FT R-space and *k*-space EXAFS, confirming the significant contribution of Ru atoms to the reactivity in OER.[70] The group of Hou, on the other hand, observed that the Ni species in the substrate of their Ru_1/D–NiFe LDH behaved dynamically during the OER process. While in oxidizing conditions with increasing applied potential, *in situ* Raman revealed that the LDH was oxidized into a γ-NiOOH species and transformed back to LDH when the potential was decreased from water oxidation conditions. Their findings suggested, that the reversible transformation between LDH and the oxyhydroxides are suggested to be the real active species. DFT calculations revealed a synergetic effect between the support and a Ru–O moiety as active sites for high rates of O_2 formation ascribing both species, the single Ru sites and the LDH substrate, which are important to enhance the OER activity.[66]

Similar findings were described by the group of Zhang and Wang for their SA Au supported on NiFe LDH (Au_1/NiFe LDH). I*n situ* Raman study at different anodic potentials OER showed the formation of NiOOH. In contrast to the aforementioned Ru_1/D-NiFe LDH, this transformation is not reversible, which was strongly supported by *ex situ* XANES analysis suggesting the *in situ* formed Au_1/NiFeOOH acts as the catalytic species during OER.[49] Not long ago, Tan et al. presented a SA Ir catalyst on nanoporous $(Ni_{0.74}Fe_{0.26})_3P$ (np-Ir/NiFeP) that is transformed and oxidized into np-Ir/NiFeO during electrochemical activation, forming a Ni(Fe)OOH surface layer. The Ir L_3-edge XANES and the corresponding FT-EXAFS spectra (Figure 8a,b) revealed the structural evolution of the catalyst during OER. Further, the variation of the Ir–O bond was also detected (Figure 8c). With increasing voltage, np-Ir/NiFeO showed an increase in valency and coordination number of Ir. This effect was observed to be reversible and the valance state of Ir was restored to its initial state when applied potential came back to OCV. Additionally, the shortening of Ir–O bonds was observed under harsh OER conditions (Figure 8b). In the case of Ni, they observed a clear oxidation of the species, as evidenced by the positive shift in the XANES spectrum (Figure 8d) and a change in the local atomic structure (Figure 8d). With increasing potential Ni further oxidizes from a hydroxide into an oxyhydroxide species, indicated by shrinking Ni–O bonds that could further stabilize isolated Ir sites on the surface and avoid aggregation during OER. Similar observations were made for the Fe species with both of the oxidation processes, for Ni and Fe being irreversible (Figure 8e).[28]

While working on non-noble metal-based SACs, Lou and Gu reported SA Ni@S/N-doped carbon as an efficient OER catalyst in alkaline conditions. They observed structural and electronic microvariations of the single Ni sites potentially driven under OER conditions showing dynamic behavior.[76] Another TM SAC prepared by the group of Kibria and Hu was based on SA Co embedded into a pyridinic N-rich graphemic network. With *operando* XAS analysis, they revealed that the square planar geometry of Co^{II} remained unchanged in the KOH solution, and with rising potential, the Co^{II} species only slightly oxidized to $Co^{II\delta+}$ due to the oxyhydroxide formation. At OCP, the Co^{II} species were again regenerated.[73]

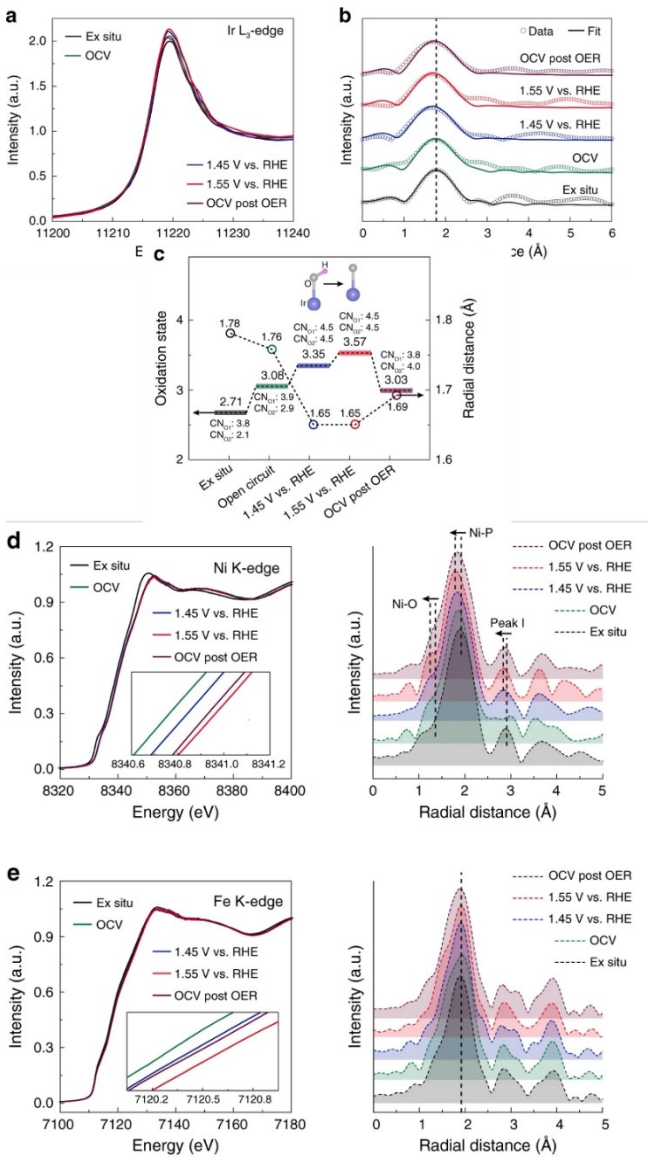

Figure 8. (a) *Operando* Ir-XANES spectra of np-Ir/NiFeO at different applied potentials, (b) Ir–O first shell FT-EXAFS showing the change in the bond distance with varying potentials, (c) the variation of the oxidation state of Ir with potential change, (d) *operando* Ni-XANES and EXAFS at different applied potentials (e) *operando* Fe-XANES and EXAFS at different applied potentials, modified with permission from ref. [28] copyright 2020, Nature Publishing Group.

In a different study, it was shown that a catalyst with a single Co site underwent significant structural changes when immersed in an alkaline electrolyte. The catalyst then underwent electrochemical activation, where it became a dimeric Co–Fe structure, which was thought to be the active site in the electrocatalytic OER. In the meantime, the group of Chen and Hu prepared the SA Co precatalyst dispersed on N-doped carbon support (Co–N–C) via wet-impregnation method, calcination, and etching. The electrochemical activation process in the Fe-containing electrolyte initiated the incorporation of Fe ions into the Co–N–C catalyst forming the Co–Fe–N–C catalyst. They noted that the carbon substrate was oxidized through electrochemically induced graphitic interlayer expansion and exfoliation, but no other morphological changes were noted. Additionally, they detected very small amounts of Co-containing np's, which were thought to play a minor role in OER activity. To investigate the structure of the catalytic species *operando* XAS was performed during activation and OER performance. During activation, the oxidation state of the Co ion in Co–N–C was close to +2, consistent with the XPS study, and after increased to +3 (Figure 9a–b). The structural feature changed from a SA into a formation of a Co-Fe double atomic catalyst, with a newly obtained scattering path (Co–Fe) indicating a Co–Fe interaction with a specific geometry in which every fourth Co ion interacted with Fe ions in Co–Fe–N–C (Figure 9a–b). This newly formed structure remained stable even after prolonged OER conditions but the number of Co-centers interacting with Fe ions increased to one-third (Figure 9c). The oxidation state increased with the advancing OER process to significantly higher than +3 consistent with a Co(IV)=O species that was regarded as the active species (Figure 9b).[128] This observation was turned into a general synthesis strategy to transform SA precatalysts into double atom electrocatalysts supported on N-doped carbon. With *in situ* studies, they revealed the mechanistic, structural, and electronic differences during OER of six analogous bimetallic catalysts containing Co, Ni, or Fe, and introduced a simple path to molecularly defined OER electrocatalysts.[129]

Controlling the metal-support interaction is a vital step in the fabrication of SACs, which is strongly dependent on the anchoring sites, which might be defects or functionalities incorporated to immobilize the metal single atoms. An in situ XAS and DFT study was conducted to determine the change in

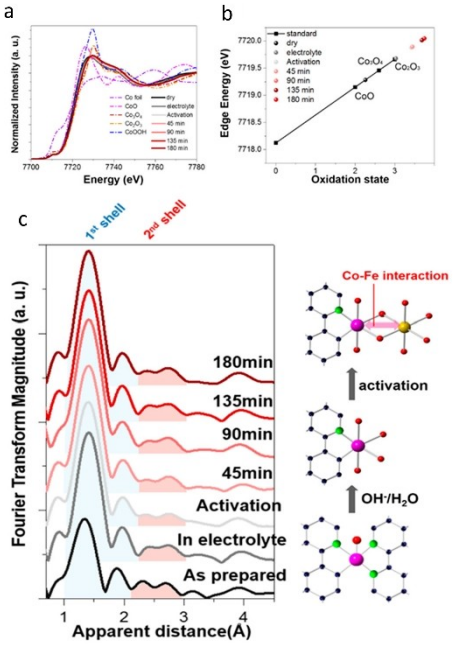

Figure 9. (a) *Operando* XANES of Co–Fe–N–C compared with the reference samples, (b) the K-edge energies of XANES, (c) Co K-edge FTEXAFS of the catalyst under various OER conditions, modified with permission from ref. [128] copyright 2019, American Chemical Society.

the structural and electronic features SA Ru on the CoFe-LDH during OER. No obvious change in the distribution state of the monatomic structure of SA Ru was observed after the long-term stability test. The XANES investigation revealed that during the OER at 1.6 V vs RHE, Ru underwent oxidation to a higher oxidation state, specifically below $+4$, compared to RuO_2. This suggests that the single atomic Ru in the Ru/CoFe-LDHs catalyst does not transition into an unstable phase of $Ru(4+\delta)+$ (with $\delta > 0$) during the OER reaction, which could lead to Ru dissolution and degradation of RuO_2-based catalysts. Interestingly, upon returning the applied potential to OCV, the Ru XANES edge shifted back to a lower energy level around the initial edge. Although the XANES edge did not precisely align with the initial OCV one, the reversible change in Ru valence state provides strong evidence of its active involvement in the catalytic reaction for OER.[26]

Similarly, in the case of the CoFe-LDH, XANES showed that Co, and Fe underwent a higher oxidation state under applied potential. However, upon reverting to OCV, there was no observable alteration in the Fe and Co edges. This contrasts with the behavior of Ru and indicates an irreversible transformation of Co and Fe, likely attributable to the robust adsorption of intermediate groups on the Co or Fe sites. All of the Co, Fe, and Ru species showed significant structural changes at potential 1.6 V. The local structures of Co and Fe, however, did not show any signs of reversibility when the electrode potential was returned to OCV.[26]

According to a model-based study, the bonding lengths of several chemical bonds were irreversibly compressed during the OER reaction. These bonds included Co–O, Co–O–Fe, Co–O–Co, Co–O–Ru, Fe–O, Fe–O–Co, and Fe–O–Ru. This bond contraction probably stabilizes the surface Ru atomic structure. During the reversible changes observed in OER, Ru did not surpass a $4+$ oxidation state, which might be explained by the improved stability of the Ru single-atom catalyst. Both operando XANES and EXAFS analyses demonstrate the reversibility of Ru and the irreversibility of Fe and Co, highlighting Ru's role as the active site in monatomic Ru/CoFe-LDHs and underscoring the significance of the support material.[26]

9. Insights Into the Active State of SACs

The compiled results remain unclear, and literature does not come to a unanimous consensus about the stability of SACs during OER. Several groups have investigated various types of noble and non-noble metal-based SACs to reveal their active sites and probe their stability under long-term conditions of OER. Noble metal catalysts are still considered to be the most active materials and will remain their significant role in electrocatalysis.[65,122,130] Therefore, downsizing them to the SA scale is a preferred strategy to maximize their use. In many cases, it was observed that the harsh oxidation processes during OER affect both the catalyst and the support material leading to their transformation either dynamically or permanently.[131] Although most of the noble metal-based catalysts such as Au, Pt, Ru, or Ir remain atomically dispersed during the OER and do not aggregate, results on the overall stability during the electrocatalytic process vary.[62,121,132] Oxidation and transformation of the substrate is an often observed phenomenon that changes the SACs permanently and often these processes are accompanied by dissolution processes of either both or one, the substrate and/or the catalytic active species.[45] Similar observations have been made for various non-noble metal-based catalysts.[115] Leaching processes of the catalytic active species as well as dynamic and permanent oxidation processes of the substrate have been observed and lead to minor changes in structure or composition.[64,133]

However, key steps involved in the mechanism of OER in SACs remain similar in many studies and have been confirmed through *in situ* measurements and DFT calculations. In the initial step, the adsorption of OH^- onto the active sites of the SACs initiates the reaction. Then, these metal atoms serve as the catalytic center and form active intermediates, such as hydroxyl (OH*) and oxy (O*) species. These active intermediates react with other OH^- to form oxygen-oxygen bonds (OOH*), leading to the formation of oxygen gas (O_2) that is finally released from the active site. This completes the OER cycle, and the single metal atom is ready to catalyze the reaction again (Figure 10a–b). While the general mechanism described above, provides a framework for understanding the OER in SACs, the specific details of the mechanism can vary depending on the metal atom, the support material, and therefore, the local environment around the catalytic site. The choice of support materials, such as carbon, metal oxides, or other substrates can influence the electronic structure and stability of the single metal atom and affect its catalytic activity. The coordination environment around the catalytic active single metal atom, including the

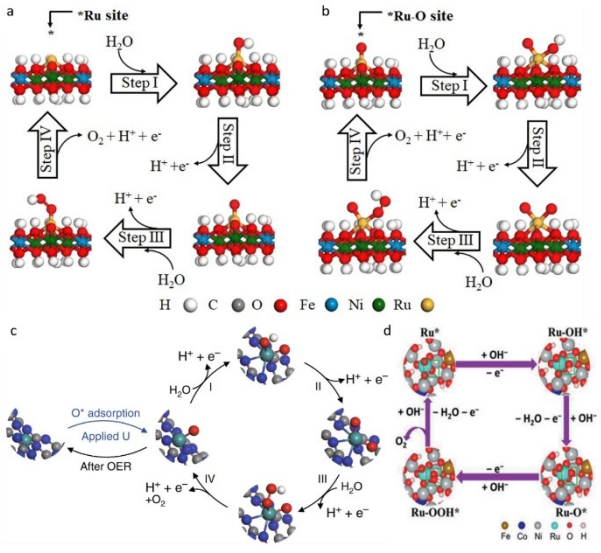

Figure 10. (a-b) Schemes for the proposed OER mechanism of Ru_1/D-NiFe LDH, reprinted with permission from ref. [66] copyright 2021, Nature Publishing Group (c) Schematic illustration of the OER mechanism of Ru–N–C catalyst. The gray atoms represent C, blue is N, red O, white is H, and light green atoms represent Ru, reprinted with permission from ref. [127] copyright 2019, Nature Publishing Group (d) Calculated OER pathway by DFT for Ru SAs/AC-FeCoNi, reprinted with permission from ref. [70] copyright 2019, Wiley-VCH.

ligands or neighboring atoms, can impact the catalytic properties and these changes in coordination can alter the adsorption energies of reaction intermediates.[129] The local surface structure, defects, and the presence of functional groups on the catalyst surface can also influence the OER mechanism. These factors may affect the binding strength of reactants and intermediates. Through in-depth *operando* XAS analysis, it has been shown that SACs exhibit variations in their reaction pathways and kinetics based on these parameters. For the Ru_1/D-NiFe LDH, it was found that the Ru–O* has a lower Gibbs free energy comparison to the Ru*, and therefore the transformed Ru–O* species was identified as the catalytic active sites. It was further shown that the formation of the OH* is the RDS for the Ru–O site (Figure 10a–b).[66] Very close to these results, a similar mechanism was developed for Ru SAC Ru–N–C by Yao et al. In their atomically dispersed Ru on nitrogen-doped carbon, the Ru–O* species was also identified as the active species with the lowest Gibbs free energy, but they concluded that the overall RDS was the formation of OOH* from O* (Figure 10c). In this case, it was shown that the formation of M–O* from the M* species is reversible and indicates an unhinged material after OER.[127]

In contrast to these results, it has been shown via *in situ* measurements and DFT calculations that the mechanism can differ drastically with different substrates. Wu and Li showed for their Ru SAs/AC-FeCoNi that Ru* sites and not Ru–O* sites have the lowest Gibbs free energy and are therefore they are the active species in their synthesized SAC. Further, they could show that the RDS is the formation of M–O* from the M-OH* species presents very different kinetic barriers for the proposed mechanism of Ru during OER (Figure 10d). Consequently, the results indicate a dynamic behavior of the Ru sites but investigations on the substrate revealed that after OER Fe, Ni, and Co have been partially oxidized.[70]

Besides the crucial role of the chemical surroundings of the SACs, different metals have distinct electronic structures and catalytic properties that influence the mechanism of OER.[28] For example, SACs based on transition metals like Fe, Co, and Ni can exhibit different behavior.[129] It has been shown that some TM SACs, can dimerize with Fe-impurities from the electrolyte and improve the catalytic efficiency,[128] and depending on the TM, the kinetics and thermodynamics of the OER mechanism can vary dramatically.[129] In contrast to the noble metal-based SACs the catalytic active species has been identified as an M* that acts as the real active center in OER. For both systems Ni and Co, the formation of the M–O* from the M-OH* intermediate has been found to be the RDS for the atomically dispersed atoms on N-doped carbon.[73,76] To properly investigate and tailor these factors to design SACs, *in situ* analysis such as Raman, XAS, XPS, etc. is unparalleled. The complex concatenation of metal support interaction, metal identity, and OER mechanism can vary dramatically for each SACs and influence the stability. Thus, to gain a detailed understanding of the specific system, time-resolved *in situ* insight is crucial for optimizing their activity, efficiency, and stability in OER.

10. Conclusion and Outlook

SACs have become prominent alternatives in heterogeneous catalysis, particularly in the field of energy applications such as water splitting. The efficiency and stability of SACs in OER are highly connected to their unique electronic and geometric properties. The isolated metal atoms provide highly active sites with distinct electronic structures, which can enhance the adsorption and activation of reactants. Understanding and optimizing the mechanisms of OER is of mere importance to develop efficient and cost-effective catalysts for water electrolysis but also for other energy applications. Achieving optimal catalytic performance and stability requires a suitable synthetic technique and a carefully selected or designed support. Despite notable progress, challenges such as large-scale preparation, ensuring high porosity, and high surface area support, persist. Due to the high surface free energy of SAs agglomeration processes occur to eventually form thermodynamically more stable clusters and even nanoparticles leading to a reduced catalytic activity. By choosing and modifying suitable substrates to create defects and vacancies for an optimal coordination environment aggregation can be prevented. Other strategies such as controlled synthesis conditions, e. g. precursor concentration, temperature, pressure, reaction time, and utilization of atomic dispersion methods such as wet impregnation, atomic layer deposition, and chemical vapor deposition can be employed to ensure atomically distributed single atom sites. Also surface passivation or functionalization with organic ligands or inorganic species, protective layers, and polymers provide suitable conditions to hinder migration and agglomeration and stabilize SAs on the support surface, especially in harsh conditions such as alkaline OER. So far only a few reported SACs perform OER at high current densities ($>$ 500 mA cm^{2-}) and prolonged conditions that surpass $>$1000 h. Most of the reported SACs show operating conditions below 500 mA cm^{2-} and often less than 100 h. To achieve industrial standards and replace traditional heterogeneous catalysts for large-scale applications, both requirements have to increase. For that reason, understanding the relationship between SACs and the substrate is crucial for enhancing and stabilizing catalytic performance. Their behavior in terms of migration and agglomeration, stability, and nature of active species, especially in harsh conditions, remains incompletely understood. The synergy between experimental and analytical data, along with theoretical calculations, is pivotal in accurately predicting structural stabilities. Only advanced techniques such as DFT and *in situ* XPS, XAFS, IR, and Raman spectroscopy can aid in the predesign of catalysts at the atomic level and are imperative to confront the challenges mentioned earlier. Although SACs exhibit promising catalytic performances, their full potential is yet to be realized. Overcoming the low loading of SACs, which is closely related to the problem of migration and agglomeration could significantly enhance the catalytic performance by providing more active sites. In this regard, synthetic methods must be improved to make SACs industrial applicable, so far cost intensive precursors, high energy methods such as ALD, or arc beam, and high-temperature pyrolysis prevent widespread

and large-scale productions, especially in high loading. Further, a deeper understanding of the interactions between the isolated atoms and the support is needed to advance in SAC synthesis. Limitations through appropriate characterization techniques, for instance, *in-situ* analysis on the atomic scale, or testing characterizing in laboratory and industrial conditions limit fast advancement towards a fundamental understanding of supported single atoms, necessary to increase loading, stability, and catalytic efficiency. With extensive research, including theoretical approaches such as DFT, and AI combined with advanced characterization techniques for detailed monitoring of catalytic reactions, it is anticipated that in the coming years, not only in the energy sector but also in various other catalytic reactions SACs will play a significant role.

Acknowledgements

The authors gratefully acknowledge support from the German Federal Ministry of Education and Research in the framework of the project Catlab (03EW0015A/B). Further, the financial support from DST/IT/DAAD/P-08/2022 (G) is genuinely appreciated as well as the financial support of DAAD Projekt-ID 57622617 of the Bundesministerium für Bildung und Forschung (BMBF). Open Access funding enabled and organized by Projekt DEAL.

Conflict of Interests

The authors declare no conflict of interest.

Data Availability Statement

Data sharing is not applicable to this article as no new data were created or analyzed in this study.

Keywords: coordination modulation · electronic interaction · in situ spectroscopy · oxygen evolution reaction · single atom catalysts

[1] Y. Chen, S. Ji, C. Chen, Q. Peng, D. Wang, Y. Li, *Joule* **2018**, *2*, 1242.
[2] Q. Wang, Z. Zhang, C. Cai, M. Wang, Z. L. Zhao, M. Li, X. Huang, S. Han, H. Zhou, Z. Feng, et al., *J. Am. Chem. Soc.* **2021**, *143*, 13605.
[3] A. Alarawi, V. Ramalingam, J.-H. He, *Mater. Today Energy* **2019**, *11*, 1.
[4] H. Zhang, X. F. Lu, Z.-P. Wu, X. W. D. Lou, *ACS Cent. Sci.* **2020**, *6*, 1288.
[5] X.-F. Yang, A. Wang, B. Qiao, J. Li, J. Liu, T. Zhang, *Acc. Chem. Res.* **2013**, *46*, 1740.
[6] Q. Zhang, J. Guan, *Adv. Funct. Mater.* **2020**, *30*, 2000768.
[7] L. Liu, A. Corma, *Chem. Rev.* **2018**, *118*, 4981.
[8] Z. Qi, Y. Zhou, R. Guan, Y. Fu, J.-B. Baek, *Adv. Mater.* **2023**, *35*, e2210575.
[9] W. Zhang, Q. Fu, Q. Luo, L. Sheng, J. Yang, *JACS Au* **2021**, *1*, 2130.
[10] X. Li, L. Liu, X. Ren, J. Gao, Y. Huang, B. Liu, *Sci. Adv.* **2020**, *6*, abb6833.
[11] V. Giulimondi, S. Mitchell, J. Pérez-Ramírez, *ACS Catal.* **2023**, *13*, 2981.
[12] H. Liu, C. Liu, X. Zong, Y. Wang, Z. Hu, Z. Zhang, *Chem. Asian J.* **2023**, *18*, e202201161.
[13] Y. Lou, J. Xu, Y. ZHANG, C. Pan, Y. Dong, Y. Zhu, *Mater. Today Nano* **2020**, *12*, 100093.
[14] H. Zhang, X. Jin, J.-M. Lee, X. Wang, *ACS Nano* **2022**, *16*, 17572.
[15] B. Qiao, A. Wang, X. Yang, L. F. Allard, Z. Jiang, Y. Cui, J. Liu, J. Li, T. Zhang, *Nat. Chem.* **2011**, *3*, 634.
[16] B. B. Sarma, F. Maurer, D. E. Doronkin, J.-D. Grunwaldt, *Chem. Rev.* **2023**, *123*, 379.
[17] C. Zhu, Q. Shi, S. Feng, D. Du, Y. Lin, *ACS Energy Lett.* **2018**, *3*, 1713.
[18] H. Fei, J. Dong, D. Chen, T. Hu, X. Duan, I. Shakir, Y. Huang, X. Duan, *Chem. Soc. Rev.* **2019**, *48*, 5207.
[19] L. Zou, Y.-S. Wei, C.-C. Hou, C. Li, Q. Xu, *Small* **2021**, *17*, e2004809.
[20] H. Zhang, W. Liu, D. Cao, D. Cheng, *iScience* **2022**, *25*, 104367.
[21] P. Aggarwal, D. Sarkar, K. Awasthi, P. W. Menezes, *Coord. Chem. Rev.* **2022**, *452*, 214289.
[22] a) X. Cui, W. Li, P. Ryabchuk, K. Junge, M. Beller, *Nat. Catal.* **2018**, *1*, 385; b) A. K. Singh, B. Singh, A. Indra, in *Single Atom Catalysts*, Elsevier, **2024**, pp. 119–146.
[23] K. Qi, M. Chhowalla, D. Voiry, *Mater. Today* **2020**, *40*, 173.
[24] S. Mitchell, J. Pérez-Ramírez, *Nat. Commun.* **2020**, *11*, 4302.
[25] X. Li, X. Yang, Y. Huang, T. Zhang, B. Liu, *Adv. Mater.* **2019**, *31*, e1902031.
[26] P. Li, M. Wang, X. Duan, L. Zheng, X. Cheng, Y. Zhang, Y. Kuang, Y. Li, Q. Ma, Z. Feng, et al., *Nat. Commun.* **2019**, *10*, 1711.
[27] J. Zhou, Z. Xu, M. Xu, X. Zhou, K. Wu, *Nanoscale Adv.* **2020**, *2*, 3624.
[28] K. Jiang, M. Luo, M. Peng, Y. Yu, Y.-R. Lu, T.-S. Chan, P. Liu, F. M. F. de Groot, Y. Tan, *Nat. Commun.* **2020**, *11*, 2701.
[29] R. Mehmood, G. Long, W. Fan, M. Li, L. Liu, F. Zhang, *J. Energy Chem.* **2023**, *79*, 410.
[30] L. Zhuang, Y. Jia, H. Liu, X. Wang, R. K. Hocking, H. Liu, J. Chen, L. Ge, L. Zhang, M. Li, et al., *Adv. Mater.* **2019**, *31*, e1805581.
[31] Z. Zhang, C. Feng, C. Liu, M. Zuo, L. Qin, X. Yan, Y. Xing, H. Li, R. Si, S. Zhou, et al., *Nat. Commun.* **2020**, *11*, 1215.
[32] J. Li, C. Chen, L. Xu, Y. Zhang, W. Wei, E. Zhao, Y. Wu, C. Chen, *JACS Au* **2023**, *3*, 736.
[33] S. Iqbal, B. Safdar, I. Hussain, K. Zhang, C. Chatzichristodoulou, *Adv. Energy Mater.* **2023**, *13*, 2203913.
[34] F. Lu, M. Zhou, Y. Zhou, X. Zeng, *Small* **2017**, *13*, 1701931.
[35] Y. Zhou, R. Lu, X. Tao, Z. Qiu, G. Chen, J. Yang, Y. Zhao, X. Feng, K. Müllen, *J. Am. Chem. Soc.* **2023**, *145*, 3647.
[36] K. Zhang, R. Zou, *Small* **2021**, *17*, e2100129.
[37] A. K. Singh, S. Ji, B. Singh, C. Das, H. Choi, P. W. Menezes, A. Indra, *Mater. Today Chem.* **2022**, *23*, 100668.
[38] A. Indra, T. Song, U. Paik, *Adv. Mater.* **2018**, *30*, e1705146.
[39] a) F.-Y. Chen, Z.-Y. Wu, Z. Adler, H. Wang, *Joule* **2021**, *5*, 1704; b) B. Singh, A. Yadav, A. Indra, *J. Mater. Chem. A* **2022**, *10*, 3843.
[40] H. Chen, X. Liang, Y. Liu, X. Ai, T. Asefa, X. Zou, *Adv. Mater.* **2020**, *32*, e2002435.
[41] B. Singh, Y.-C. Huang, A. Priyadarsini, P. Mannu, S. Dey, G. K. Lahiri, B. S. Mallik, C.-L. Dong, A. Indra, *J. Mater. Chem. A* **2023**, *11*, 15906.
[42] B. Singh, A. Singh, A. Yadav, A. Indra, *Coord. Chem. Rev.* **2021**, *447*, 214144.
[43] F. Song, L. Bai, A. Moysiadou, S. Lee, C. Hu, L. Liardet, X. Hu, *J. Am. Chem. Soc.* **2018**, *140*, 7748.
[44] L. Wu, T. Guo, T. Li, *iScience* **2021**, *24*, 102398.
[45] Y. Yang, Q.-N. Yang, Y.-B. Yang, P.-F. Guo, W.-X. Feng, Y. Jia, K. Wang, W.-T. Wang, Z.-H. He, Z.-T. Liu, *ACS Catal.* **2023**, *13*, 2771.
[46] D. Zhang, Q. Zhang, C. Peng, Z. Long, G. Zhuang, D. Kramer, S. Komarneni, C. Zhi, D. Xue, *iScience* **2023**, *26*, 106624.
[47] H. Fei, J. Dong, Y. Feng, C. S. Allen, C. Wan, B. Volosskiy, M. Li, Z. Zhao, Y. Wang, H. Sun, et al., *Nat. Catal.* **2018**, *1*, 63.
[48] Y. Zheng, Y. Jiao, Y. Zhu, Q. Cai, A. Vasileff, L. H. Li, Y. Han, Y. Chen, S.-Z. Qiao, *J. Am. Chem. Soc.* **2017**, *139*, 3336.
[49] a) J. Zhang, J. Liu, L. Xi, Y. Yu, N. Chen, S. Sun, W. Wang, K. M. Lange, B. Zhang, *J. Am. Chem. Soc.* **2018**, *140*, 3876; b) F. Wang, P. Zou, Y. Zhang, W. Pan, Y. Li, L. Liang, C. Chen, H. Liu, S. Zheng, *Nat. Commun.* **2023**, *14*, 6019.
[50] J. Zhu, L. Cai, X. Yin, Z. Wang, L. Zhang, H. Ma, Y. Ke, Y. Du, S. Xi, A. T. S. Wee, et al., *ACS Nano* **2020**, *14*, 5600.
[51] a) Y.-C. Zhang, C. Han, J. Gao, L. Pan, J. Wu, X.-D. Zhu, J.-J. Zou, *ACS Catal.* **2021**, *11*, 12485; b) A. K. Singh, S. Ji, B. Singh, C. Das, H. Choi, P. W. Menezes, A. Indra, *Mater. Today Chem.* **2022**, *23*, 100668.
[52] a) B. Singh, P. Mannu, Y.-C. Huang, R. Prakash, S. Shen, C.-L. Dong, A. Indra, *Angew. Chem. Int. Ed.* **2022**, *61*, e202211585; b) P. Maurya, V. Vyas, A. N. Singh, A. Indra, *Chem. Commun.* **2023**, *59*, 7200.
[53] S. Gong, T. Zhang, J. Meng, W. Sun, Y. Tian, *Mater. Chem. Front.* **2024**, *8*, 603.
[54] X. Wang, H. Zhong, S. Xi, W. S. V. Lee, J. Xue, *Adv. Mater.* **2022**, *34*, e2107956.

[55] X. Guo, H. Zhang, Z. Shen, X. Liu, W. Xia, M. Ma, D. Cao, *Small Structures* **2023**, *4*, 2300081.
[56] a) S. Anantharaj, S. R. Ede, K. Sakthikumar, K. Karthick, S. Mishra, S. Kundu, *ACS Catal.* **2016**, *6*, 8069; b) S. Li, E. Li, X. An, X. Hao, Z. Jiang, G. Guan, *Nanoscale* **2021**, *13*, 12788; c) T. Pain, A. K. Singh, A. Tarai, S. Mondal, A. Indra, S. Kar, *Inorg. Chem.* **2023**, *62*, 18779; d) A. Banerjee, M. K. Awasthi, P. Maji, M. Pal, S. T. Aziz, G. K. Lahiri, A. Dutta, *ChemElectroChem* **2023**, *10*, e202201098; e) H. Wang, M. Zhou, P. Choudhury, H. Luo, *Appl. Mater. Today* **2019**, *16*, 56; f) J. Li, C. A. Triana, W. Wan, D. P. Adiyeri Saseendran, Y. Zhao, S. E. Balaghi, S. Heidari, G. R. Patzke, *Chem. Soc. Rev.* **2021**, *50*, 2444; g) A. Indra, U. Paik, T. Song, *Angew. Chem. Int. Ed.* **2018**, *57*, 1241; h) P. W. Menezes, A. Indra, A. Bergmann, P. Chernev, C. Walter, H. Dau, P. Strasser, M. Driess, *J. Mater. Chem. A* **2016**, *4*, 10014; i) P. W. Menezes, A. Indra, V. Gutkin, M. Driess, *Chem. Commun.* **2017**, *53*, 8018; j) P. W. Menezes, A. Indra, C. Das, C. Walter, C. Göbel, V. Gutkin, D. Schmeißer, M. Driess, *ACS Catal.* **2017**, *7*, 103; k) S. Dutta, A. Indra, Y. Feng, T. Song, U. Paik, *ACS Appl. Mater. Interfaces.* **2017**, *9*, 33766.
[57] Y. Yang, Y. Yang, Z. Pei, K.-H. Wu, C. Tan, H. Wang, L. Wei, A. Mahmood, C. Yan, J. Dong, et al., *Matter* **2020**, *3*, 1442.
[58] Y. Zhou, J. Li, X. Gao, W. Chu, G. Gao, L.-W. Wang, *J. Mater. Chem. A* **2021**, *9*, 9979.
[59] C. Zhu, S. Fu, Q. Shi, D. Du, Y. Lin, *Angew. Chem. Int. Ed.* **2017**, *56*, 13944.
[60] L. Jiao, H.-L. Jiang, *Chem* **2019**, *5*, 786.
[61] X. Wang, L. Sun, W. Zhou, L. Yang, G. Ren, H. Wu, W.-Q. Deng, *Cell Reports Phys. Sci.* **2022**, *3*, 100804.
[62] Z. Lei, W. Cai, Y. Rao, K. Wang, Y. Jiang, Y. Liu, X. Jin, J. Li, Z. Lv, S. Jiao, et al., *Nat. Commun.* **2022**, *13*, 24.
[63] C. Cai, S. Han, Q. Wang, M. Gu, *ACS Nano* **2019**, *13*, 8865.
[64] J. Yan, L. Kong, Y. Ji, J. White, Y. Li, J. Zhang, P. An, S. Liu, S.-T. Lee, T. Ma, *Nat. Commun.* **2019**, *10*, 2149.
[65] D. Cao, Z. Zhang, Y. Cui, R. Zhang, L. Zhang, J. Zeng, D. Cheng, *Angew. Chem. Int. Ed.* **2023**, *62*, e202214259.
[66] P. Zhai, M. Xia, Y. Wu, G. Zhang, J. Gao, B. Zhang, S. Cao, Y. Zhang, Z. Li, Z. Fan, et al., *Nat. Commun.* **2021**, *12*, 4587.
[67] J. Guo, H. Liu, D. Li, J. Wang, X. Djitcheu, D. He, Q. Zhang, *RSC Adv.* **2022**, *12*, 9373.
[68] Q. He, S. Qiao, Q. Zhou, Y. Zhou, H. Shou, P. Zhang, W. Xu, D. Liu, S. Chen, X. Wu, et al., *Nano Lett.* **2022**, *22*, 3832.
[69] C. Walter, P. W. Menezes, in *Single Atom Catalysts*, Elsevier, **2024**, pp. 35–67.
[70] Y. Hu, G. Luo, L. Wang, X. Liu, Y. Qu, Y. Zhou, F. Zhou, Z. Li, Y. Li, T. Yao, et al., *Adv. Energy Mater.* **2021**, *11*, 2002816.
[71] a) H.-W. Liang, S. Brüller, R. Dong, J. Zhang, X. Feng, K. Müllen, *Nat. Commun.* **2015**, *6*, 7992; b) S. Yang, J. Kim, Y. J. Tak, A. Soon, H. Lee, *Angew. Chem. Int. Ed.* **2016**, *55*, 2058; c) R.-Q. Zhang, T.-H. Lee, B.-D. Yu, C. Stampfl, A. Soon, *Phys. Chem. Chem. Phys.* **2012**, *14*, 16552.
[72] F. D. Speck, J. H. Kim, G. Bae, S. H. Joo, K. J. J. Mayrhofer, C. H. Choi, S. Cherevko, *JACS Au* **2021**, *1*, 1086.
[73] P. Kumar, K. Kannimuthu, A. S. Zeraati, S. Roy, X. Wang, X. Wang, S. Samanta, K. A. Miller, M. Molina, D. Trivedi, et al., *J. Am. Chem. Soc.* **2023**, *145*, 8052.
[74] S. Ma, W. Han, W. Han, F. Dong, Z. Tang, *J. Mater. Chem. A* **2023**, *11*, 3315.
[75] Q. Wang, C.-Q. Xu, W. Liu, S.-F. Hung, H. Bin Yang, J. Gao, W. Cai, H. M. Chen, J. Li, B. Liu, *Nat. Commun.* **2020**, *11*, 4246.
[76] Y. Zhao, X. F. Lu, G. Fan, D. Luan, X. Gu, X. W. D. Lou, *Angew. Chem. Int. Ed.* **2022**, *61*, e202212542.
[77] P. Tieu, X. Yan, M. Xu, P. Christopher, X. Pan, *Small* **2021**, *17*, e2006482.
[78] W. H. Lee, Y.-J. Ko, J.-Y. Kim, B. K. Min, Y. J. Hwang, H.-S. Oh, *Chem. Commun.* **2020**, *56*, 12687.
[79] L. Zhou, S.-Y. Lu, S. Guo, *SusMat* **2021**, *1*, 194.
[80] Q. Liu, Z. Zhang, *Catal. Sci. Technol.* **2019**, *9*, 4821.
[81] P. Qi, J. Wang, X. Djitcheu, D. He, H. Liu, Q. Zhang, *RSC Adv.* **2021**, *12*, 1216.
[82] C. Ye, N. Zhang, D. Wang, Y. Li, *Chem. Commun.* **2020**, *56*, 7687.
[83] Y. Ding, A. Klyushin, X. Huang, T. Jones, D. Teschner, F. Girgsdies, T. Rodenas, R. Schlögl, S. Heumann, *Angew. Chem. Int. Ed.* **2018**, *57*, 3514.
[84] Y. Lin, M. Zhou, X. Tai, H. Li, X. Han, J. Yu, *Matter* **2021**, *4*, 2309.
[85] H. Zhang, G. Liu, L. Shi, J. Ye, *Adv. Energy Mater.* **2018**, *8*, 1701343.
[86] J. Y. Zhang, J. Hwang, B. J. Isaac, S. Stemmer, *Sci. Rep.* **2015**, *5*, 12419.
[87] N. D. Browning, C. Aydin, J. Lu, A. Kulkarni, N. L. Okamoto, V. Ortalan, B. W. Reed, A. Uzun, B. C. Gates, *ChemCatChem* **2013**, *5*, 2673.
[88] C. Chen, M. Sun, K. Wang, Y. Li, *SmartMat* **2022**, *3*, 533.
[89] R. F. Egerton, *Rep. Prog. Phys.* **2009**, *72*, 16502.
[90] J. Shan, C. Ye, Y. Jiang, M. Jaroniec, Y. Zheng, S.-Z. Qiao, *Sci. Adv.* **2022**, *8*, eabo0762.
[91] J. Cao, T. Mou, B. Mei, P. Yao, C. Han, X. Gong, P. Song, Z. Jiang, T. Frauenheim, J. Xiao, et al., *Angew. Chem. Int. Ed.* **2023**, *62*, e202310973.
[92] J. Timoshenko, B. Roldan Cuenya, *Chem. Rev.* **2021**, *121*, 882.
[93] M. Kottwitz, Y. Li, H. Wang, A. I. Frenkel, R. G. Nuzzo, *Chemistry Methods* **2021**, *1*, 278.
[94] J. Duan, S. Chen, M. Jaroniec, S. Z. Qiao, *ACS Catal.* **2015**, *5*, 5207.
[95] Z. Zhang, C. Feng, D. Wang, S. Zhou, R. Wang, S. Hu, H. Li, M. Zuo, Y. Kong, J. Bao, et al., *Nat. Commun.* **2022**, *13*, 2473.
[96] Z. Wang, S.-M. Xu, Y. Xu, L. Tan, X. Wang, Y. Zhao, H. Duan, Y.-F. Song, *Chem. Sci.* **2019**, *10*, 378.
[97] L. Zhang, Y. Jia, G. Gao, X. Yan, N. Chen, J. Chen, M. T. Soo, B. Wood, D. Yang, A. Du, et al., *Chem* **2018**, *4*, 285.
[98] Y. Zhu, J. Wang, J. Ma, *Small Science* **2023**, *3*.
[99] M. Liu, Y. Ji, Y. Li, P. An, J. Zhang, J. Yan, S. F. Liu, *Small* **2021**, *17*, e2102448.
[100] C. Lin, Y. Zhao, H. Zhang, S. Xie, Y.-F. Li, X. Li, Z. Jiang, Z.-P. Liu, *Chem. Sci.* **2018**, *9*, 6803.
[101] M.-Q. Yang, K.-L. Zhou, C. Wang, M.-C. Zhang, C.-H. Wang, X. Ke, G. Chen, H. Wang, R.-Z. Wang, *J. Mater. Chem. A* **2022**, *10*, 25692.
[102] N. Yang, S. Tian, Y. Feng, Z. Hu, H. Liu, X. Tian, L. Xu, C. Hu, J. Yang, *Small* **2023**, *19*, e2207253.
[103] T. Pu, W. Zhang, M. Zhu, *Angew. Chem. Int. Ed.* **2023**, *62*, e202212278.
[104] Z. Shi, Y. Wang, J. Li, X. Wang, Y. Wang, Y. Li, W. Xu, Z. Jiang, C. Liu, W. Xing, et al., *Joule* **2021**, *5*, 2164.
[105] Q. Wang, X. Huang, Z. L. Zhao, M. Wang, B. Xiang, J. Li, Z. Feng, H. Xu, M. Gu, *J. Am. Chem. Soc.* **2020**, *142*, 7425.
[106] a) Y. Wang, D. Yan, S. El Hankari, Y. Zou, S. Wang, *Adv. Sci.* **2018**, *5*, 1800064; b) X. Long, Z. Wang, S. Xiao, Y. An, S. Yang, *Mater. Today* **2016**, *19*, 213.
[107] J. Jin, X. Han, Y. Fang, Z. Zhang, Y. Li, T. Zhang, A. Han, J. Liu, *Adv. Funct. Mater.* **2022**, *32*, 2109218.
[108] D. Zhou, P. Li, X. Lin, A. McKinley, Y. Kuang, W. Liu, W.-F. Lin, X. Sun, X. Duan, *Chem. Soc. Rev.* **2021**, *50*, 8790.
[109] D. Tyndall, M. J. Craig, L. Gannon, C. McGuinness, N. McEvoy, A. Roy, M. García-Melchor, M. P. Browne, V. Nicolosi, *J. Mater. Chem. A* **2023**, *11*, 4067.
[110] D. Wang, Q. Li, C. Han, Q. Lu, Z. Xing, X. Yang, *Nat. Commun.* **2019**, *10*, 3899.
[111] >a) C. Dong, X. Zhang, J. Xu, R. Si, J. Sheng, J. Luo, S. Zhang, W. Dong, G. Li, W. Wang, et al., *Small* **2020**, *16*, e1905328>; b) Y. Zhang, C. Wu, H. Jiang, Y. Lin, H. Liu, Q. He, S. Chen, T. Duan, L. Song, *Adv. Mater.* **2018**, *30*, 1707522.
[112] X. Zheng, J. Tang, A. Gallo, J. A. Garrido Torres, X. Yu, C. J. Athanitis, E. M. Been, P. Ercius, H. Mao, S. C. Fakra, et al., *Proc. Nat. Acad. Sci.* **2021**, *118*, e2101817118.
[113] a) Y. Ou, L. P. Twight, B. Samanta, L. Liu, S. Biswas, J. L. Fehrs, N. A. Sagui, J. Villalobos, J. Morales-Santelices, D. Antipin, et al., *Nat. Commun.* **2023**, *14*, 7688; b) B. Zhang, L. Wang, Z. Cao, S. M. Kozlov, García de Arquer, F. Pelayo, C. T. Dinh, J. Li, Z. Wang, X. Zheng, L. Zhang, et al., *Nat. Catal.* **2020**, *3*, 985.
[114] L. Wang, W.-W. Tian, W. Zhang, F. Yu, Z.-Y. Yuan, *Appl. Catal. B* **2023**, *338*, 123043.
[115] H. Zhang, Y. Liu, T. Chen, J. Zhang, J. Zhang, X. W. D. Lou, *Adv. Mater.* **2019**, *31*, e1904548.
[116] Y. Li, Z.-S. Wu, P. Lu, X. Wang, W. Liu, Z. Liu, J. Ma, W. Ren, Z. Jiang, X. Bao, *Adv. Sci.* **2020**, *7*, 1903089.
[117] Y. Zhang, J. Yang, R. Ge, J. Zhang, J. M. Cairney, Y. Li, M. Zhu, S. Li, W. Li, *Coord. Chem. Rev.* **2022**, *461*, 214493.
[118] R. Qin, P. Liu, G. Fu, N. Zheng, *Small Methods* **2018**, *2*, 1700286.
[119] H. Su, X. Zhao, W. Cheng, H. Zhang, Y. Li, W. Zhou, M. Liu, Q. Liu, *ACS Energy Lett.* **2019**, *4*, 1816.
[120] Z. Li, Z. Wang, S. Xi, X. Zhao, T. Sun, J. Li, W. Yu, H. Xu, T. S. Herng, X. Hai, et al., *ACS Nano* **2021**, *15*, 7105.
[121] X. Zhao, P. Gao, Y. Yan, X. Li, Y. Xing, H. Li, Z. Peng, J. Yang, J. Zeng, *J. Mater. Chem. A* **2017**, *5*, 20202.
[122] X. Luo, X. Wei, H. Zhong, H. Wang, Y. Wu, Q. Wang, W. Gu, M. Gu, S. P. Beckman, C. Zhu, *ACS Appl. Mater. Interfaces* **2020**, *12*, 3539.
[123] P. W. Menezes, D. Sarkar, K. Awasthi, (Eds.) *Single atom catalysts: Design, synthesis, characterization, and applications in energy*, Elsevier BV, **2024**.
[124] a) B. Dasgupta, J. N. Hausmann, R. Beltrán-Suito, S. Kalra, K. Laun, I. Zebger, M. Driess, P. W. Menezes, *Small* **2023**, *19*, e2301258; b) C.

Walter, S. Kalra, R. Beltrán-Suito, M. Schwarze, P. W. Menezes, M. Driess, *Mater. Today Chem.* **2022**, *24*, 100905; c) C. Walter, P. W. Menezes, S. Orthmann, J. Schuch, P. Connor, B. Kaiser, M. Lerch, M. Driess, *Angew. Chem. Int. Ed.* **2018**, *57*, 698; d) J. N. Hausmann, R. A. Khalaniya, C. Das, I. Remy-Speckmann, S. Berendts, A. V. Shevelkov, M. Driess, P. W. Menezes, *Chem. Commun.* **2021**, *57*, 2184; e) J. N. Hausmann, S. Mebs, K. Laun, I. Zebger, H. Dau, P. W. Menezes, M. Driess, *Energy Environ. Sci.* **2020**, *13*, 3607; f) P. W. Menezes, S. Yao, R. Beltrán-Suito, J. N. Hausmann, P. V. Menezes, M. Driess, *Angew. Chem. Int. Ed.* **2021**, *60*, 4690.

[125] C. Walter, P. W. Menezes, *Synthesis techniques for single-atom catalysts*, Elsevier, **2024**.

[126] X. Li, L. Liu, X. Ren, J. Gao, Y. Huang, B. Liu, *Sci. Adv.* **2020**, *6*.

[127] L. Cao, Q. Luo, J. Chen, L. Wang, Y. Lin, H. Wang, X. Liu, X. Shen, W. Zhang, W. Liu, et al., *Nat. Commun.* **2019**, *10*, 4849.

[128] L. Bai, C.-S. Hsu, D. T. L. Alexander, H. M. Chen, X. Hu, *J. Am. Chem. Soc.* **2019**, *141*, 14190.

[129] L. Bai, C.-S. Hsu, D. T. L. Alexander, H. M. Chen, X. Hu, *Nat. Energy* **2021**, *6*, 1054.

[130] Y. Zhang, C. Wu, H. Jiang, Y. Lin, H. Liu, Q. He, S. Chen, T. Duan, L. Song, *Adv. Mater.* **2018**, *30*, e1707522.

[131] a) Q. Wang, X. Huang, Z. L. Zhao, M. Wang, B. Xiang, J. Li, Z. Feng, H. Xu, M. Gu, *J. Am. Chem. Soc.* **2020**, *142*, 7425; b) S.-Y. Lu, B. Huang, M. Sun, M. Luo, M. Jin, H. Yang, Q. Zhang, H. Liu, P. Zhou, Y. Chao, et al., *Nat. Synth* **2023**.

[132] L. Zeng, Z. Zhao, F. Lv, Z. Xia, S.-Y. Lu, J. Li, K. Sun, K. Wang, Y. Sun, Q. Huang, et al., *Nat. Commun.* **2022**, *13*, 3822.

[133] a) C. Wu, X. Zhang, Z. Xia, M. Shu, H. Li, X. Xu, R. Si, A. I. Rykov, J. Wang, S. Yu, et al., *J. Mater. Chem. A* **2019**, *7*, 14001; b) X. Han, X. Ling, D. Yu, D. Xie, L. Li, S. Peng, C. Zhong, N. Zhao, Y. Deng, W. Hu, *Adv. Mater.* **2019**, *31*, e1905622.

Manuscript received: February 17, 2024
Revised manuscript received: May 21, 2024
Version of record online: August 30, 2024